energies

Article

Performance Enhancement of a Building-Integrated Photovoltaic/Thermal System Coupled with an Air Source Heat Pump

Edward Vuong [1], Alan S. Fung [2,*] and Rakesh Kumar [2]

[1] Construction Research Centre, National Research Council of Canada, Ottawa, ON K1A 0R6, Canada
[2] Department of Mechanical, Industrial and Mechatronics Engineering, Toronto Metropolitan University, 350 Victoria St, Toronto, ON M5B 2K3, Canada
* Correspondence: alanfung@torontomu.ca

Abstract: This study explores the improvement of building integrated photovoltaic–thermal (BIPV/T) systems and their integration with air source heat pumps (ASHPs). The BIPV/T collector needs a method to effectively extract the heat it collects, while ASHP can boost their efficiency utilizing preheated air from the BIPV/T collectors. Combining these two systems presents a valuable opportunity to enhance their performance. This paper discusses technological improvements and integration through a comprehensive modelling analysis. Two versions of the BIPV/T systems were assessed using a modified version of EnergyPlus V8.0, a building energy simulation program. This study involved sensitivity analysis of the internal channel surface and cover emissivity parameters of the opaque BIPV/T (OBIPV/T), transparent BIPV/T (TBIPV/T), and building-integrated solar air heater collectors (BISAHs). Various arrangements of the collectors were also studied. A BIPV/T-BISAH array design was selected based on the analysis, and its integration with a net-zero energy house. The BIPV/T-BISAH coupled ASHP system decreased space heating electricity consumption by 6.5% for a net-zero house. These modest savings are mainly attributed to the passive design of the houses, which reduced heating loads during sunny hours/days.

Keywords: building integrated photovoltaic–thermal; solar air heater; air source heat pump; EnergyPlus modelling; thermal energy; sustainable house

check for updates

Academic Editor: George Kosmadakis

Received: 31 October 2024
Revised: 13 December 2024
Accepted: 20 December 2024
Published: 24 December 2024

Citation: Vuong, E.; Fung, A.S.; Kumar, R. Performance Enhancement of a Building-Integrated Photovoltaic/Thermal System Coupled with an Air Source Heat Pump. *Energies* **2025**, *18*, 12. https://doi.org/10.3390/en18010012

1. Introduction

Space heating makes up 63% of energy consumption in Canadian residential buildings, accounting for 17% of the country's energy usage and generating 14% of annual greenhouse gas (GHG) emissions [1,2]. These emissions come from off-site electricity generation using fossil fuels and the on-site combustion of natural gas for space and domestic hot water heating. Building energy standards have become more stringent over time to reduce GHG emissions and heating costs and have improved with objectives to minimize environmental impact and support the integration of solar energy into building envelopes [3]. Canada's 2020 national model codes aim to build all new buildings to net-zero energy-ready standards by 2030 [4]. Energy-efficient buildings are equipped with state-of-the-art technologies like heat pumps, heat recovery systems, and renewable energy integration to reduce the energy demand and GHG emissions [5,6]. This study explores the potential of building-integrated photovoltaic–thermal (BIPV/T) systems with heat pumps in a futuristic building design.

Building-integrated photovoltaic–thermal (BIPV/T) systems combine photovoltaic (PV) and solar thermal energy into a single, integrated unit [7,8]. These systems are designed to be part of the building envelope and serve dual purposes, generating electricity and capturing thermal energy, thereby maximizing solar energy harnessing per unit surface area. Benefits of BIPV/T systems include offsetting the cost of the construction of new buildings by substituting for conventional roofing/wall/window materials, increasing the electrical efficiency of the solar cells, and providing low-grade thermal energy to reduce space and/or water heating [9]. Most studies on photovoltaic–thermal collectors focus on optimizing the design, with limited consideration given to their market prospect and integration with other heating technologies, such as heat pump systems [10].

On the other hand, air source heat pumps (ASHPs) have become an emerging heating option [11]. However, ASHPs performance diminishes when operating with low-temperature ambient air sources. This problem can be alleviated by allowing the ASHPs to use preheated air from a BIPV/T system. The preheated air enables the ASHPs to operate during extremely cold-weather conditions and increases the system's Coefficient of Performance (COP). Kamel and Fung [12] showed that ASHP has the potential to meet space heating needs without extra auxiliary heat sources when combined with a BIPV/T system. The preheated air flowrate varies per the house's heating demand and the amount of solar irradiance on the BIPV/T collectors. Zhao et al. [13] found that increasing the flowrate in a BIPV/T system resulted in lower collector exit temperatures but increased the thermal output. Payne et al. [14] conducted experimental studies on the performance of a residential heat pump. It has been stated that increasing the mass flowrate of the circulating fluid in BIPV/T systems can improve their overall efficiencies up to a certain point. Beyond this point, however, it can lead to higher costs and increased energy consumption, ultimately resulting in inferior performance. Bergene and Lovvik [15] discovered that the system efficiency only increased by 1% when the flowrate was raised from 0.001 to 0.075 kg/s. One of the objectives of this study was to assess the impact of the flowrate on the energy delivered by an integrated heating system with BIPV/T collectors.

Most studies have focused on the energy savings associated with improving the performance of BIPV/T and solar air collectors through thermal and optical enhancements. However, these studies have not examined these enhancements and their impact on the hydraulic efficiency of the systems under Canadian winter conditions. The primary objective of this study was to determine how enhancements of BIPV/T systems would improve their performance in cold-weather applications.

This paper presents models and enhancements of two different BIPV/T collectors and a building integrated solar air eater (BISAH), the impact of the collector/air heater's placements in a combined BIPV/T-BISAH configuration, and the integration of a BIPV/T-BISAH with an ASHP that features source-side air flow modulation. In the following sections, the models and the parametric analyses undertaken are described, the heat transfer of the enhancements are discussed, and the results of a net-zero-ready house operating with a BIPV/T-BISAH-ASHP integrated system are presented as a case study. This research provides insights into the heat transfer characteristics of these individual and integrated systems in residential houses.

2. Methodology

This investigation explores ways to enhance the thermal and electrical performance of BIPV/T systems while preserving hydraulic efficiency. Multi-objective models were created to simulate BIPV/T collectors, a BISAH, and their integration with an ASHP; these models allow the following:

- Parametric analyses of hydraulically neutral enhancements.
- The simulation of collector arrangements (combining a BIPV/T and BISAH in a row).
- Integration with an ASHP that captures the impact of air flow modulation through a BIPV/T-BISAH array.

Key areas of this study include the emissivity of air channel surfaces, the emissivity of the collector's glass cover, a performance comparison between opaque (OBIPV/T) and transparent (TBIPV/T) BIPV/T systems, and the placement of collectors within BIPV/T-BISAH systems. The latter part of this study also looked at varying the flowrate of the BIPV/T–BISAH system to improve the overall efficiency of the BIPV/T-BISAH-ASHP system.

The original version of EnergyPlus V8.0 [16] did not include BIPV/T, BISAH, or an ASHP model that permits preheated air sources; therefore, a modified version of EnergyPlus V8.0 was developed to model the BIPV/T-BISAH-ASHP system. Existing quasi-steady models of OBIPV/T [12] were modified to include a Photovoltaic (PV) cell packing factor (PF) to parameterize the effect of the PV cell-to-collector area ratio. This resulted in the OBIPV/T and TBIPV/T models used in the present study. Two-dimensional representations of the OBIPV/T, TBIPV/T, and BISAH are shown in Figure 1.

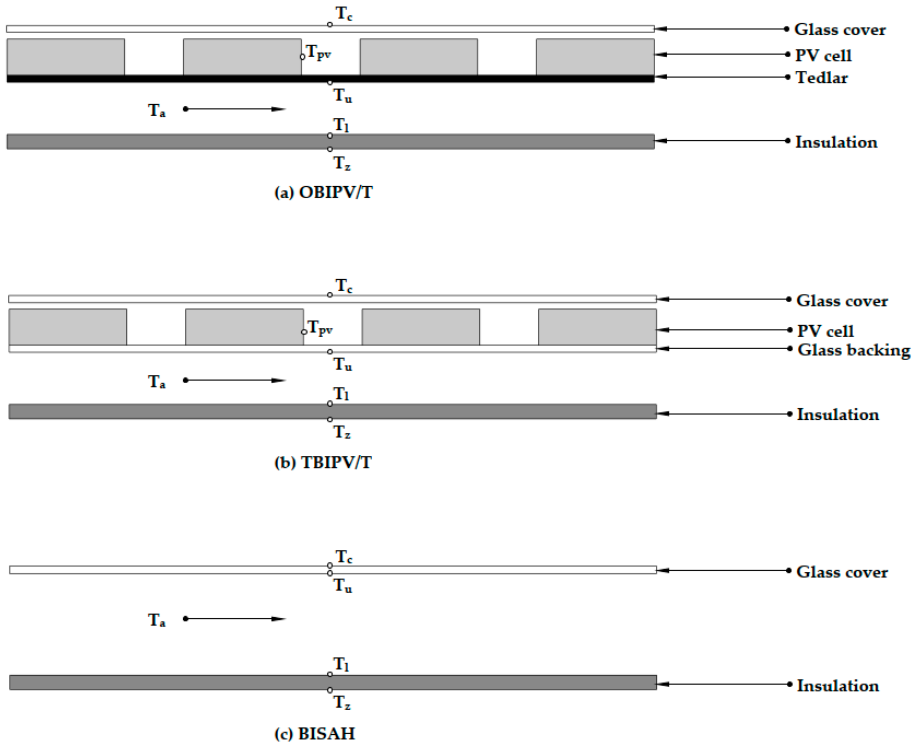

Figure 1. Schematics of (**a**) OBIPV/T, (**b**) TBIPV/T, and (**c**) BISAH.

2.1. OBIPV/T Collector Energy Balance

The energy balances below reference Figure 1a. The model was developed with the following assumptions: one-dimensional air flow, non-negligible capacitance of the air, temperature gradients along the direction of the air flow, uniform material properties, one-dimensional steady-state heat transfer, convective heat transfer coefficients at the channel surfaces based the average air temperature collector, and negligible longwave radiation between the glass cover and nearby structures.

For the top glass cover,

$$\frac{T_{pv} - T_c}{R_g} = h_c(T_c - T_{amb}) + h_{rs}\left(T_c - T_{sky}\right) \quad (1)$$

where T_{pv}, T_c, T_{amb}, and T_{sky} are the temperatures of the PV cell, glass cover, ambient air, and sky, respectively; h_c is the convective heat transfer coefficient of the wind on the cover; h_{rs} is the radiative heat transfer coefficient for the cover and the sky; and R_g is R-value of glazing.

For the PV cell layer,

$$S = \frac{T_{pv} - T_c}{R_g} + \frac{T_{pv} - T_u}{R_{pv-u}} \tag{2}$$

where S is the net absorbed solar thermal flux at the PV layer for an OBIPV/T, T_u is the temperature of the upper surface of the air channel, and R_{pv-u} is the R-value measured from the PV surface to the upper channel surface (PV cells and tedlar layer); the other parameters are defined in Equation (1).

For the upper surface of the air channel,

$$\frac{T_{pv} - T_u}{R_{pv-u}} = h_a(T_u - T_a) + h_{rad,\ u-l}(T_u - T_l) \tag{3}$$

where h_a is the convective heat transfer coefficient to air within the channel; $h_{rad,\ u-l}$ is the radiative heat transfer coefficient between the collector air channel's upper and lower surface; and T_l is the temperature of the lower channel surface.

For the air flow,

$$q = h_a(T_u - T_a) - h_a(T_a - T_l) \tag{4}$$

where q is the heat flux to air stream in the collector.

For the lower surface of the air channel,

$$h_a(T_a - T_l) + h_{rad,u-l}(T_u - T_l) = \frac{T_l - T_z}{R_{ins}} \tag{5}$$

where T_z is the temperature of the interior zone surface; and R_{ins} is the R-value of roof insulation.

The estimation of the net absorbed solar thermal flux, S, is the thermal power flux available after a portion has been deducted for PV electricity generation, E_{pv}. Expressions S and E_{pv}, as written by Kamel and Fung [12], are in Equations (6) and (7), followed by further definitions of terms and products (Equations (8) and (9)). The inclusion of the PF requires modifications to these equations, presented in Equations (10) and (12).

$$E_{pv} = (\tau\alpha)_T I_T A_{panel} \eta_{pv} \tag{6}$$

$$S = (\tau\alpha)_T I_T (1 - \eta_{pv}) \tag{7}$$

where $(\tau\alpha)_T$ is the transmittance–absorptance product for the total radiation on a surface; I_T is the total irradiance on a tilted surface; A_{panel} is the panel surface area; and η_{pv} is the efficiency of PV cells. The product $(\tau\alpha)_T\ I_T$ is the solar radiation absorbed by the panel after transmission through a single glazed layer (before deducting for electrical generation) and is expressed as

$$(\tau\alpha)_T\ I_T = (\tau\alpha)_B I_B + (\tau\alpha)_S I_S + (\tau\alpha)_{GR} I_{GR} \tag{8}$$

where I_B, I_S, and I_{GR} are the beam, sky diffuse, and ground diffuse solar irradiance components. $(\tau\alpha)_B$, $(\tau\alpha)_S$, and $(\tau\alpha)_{GR}$ are the transmittance–absorptance products of

the corresponding components of the total solar radiation; each component is estimated using Equation (9):

$$(\tau\alpha)_x = e^{-(Kl_g/cos\theta_{r,x})}\left[1 - \frac{1}{2}\left(\frac{sin^2(\theta_{r,x}-\theta_x)}{sin^2(\theta_{r,x}+\theta_x)} + \frac{tan^2(\theta_{r,x}-\theta_x)}{tan^2(\theta_{r,x}+\theta_x)}\right)\right] \quad (9)$$

where K and l_g are the glazing extinction coefficient (1/m) and glazing thickness (m), respectively. θ_x is the incident radiation angle for a solar component x (beam, sky, diffuse, or ground diffuse), and $\theta_{r,x}$ is the refractive angle for a particular solar component x.

The inclusion of a PV cell packing factor, PF, in the OBIPV/T model allows for a comparison of two same-sized collectors, but with a different number of PV cells. The electricity generated and the net absorbed solar thermal irradiance are rewritten as follows [17]:

$$E_{pv} = (\tau\alpha)_T I_T A_{PVcell}\eta_{pv} \quad (10)$$

$$S = (\tau\alpha)_T I_T - (\tau\alpha)_T I_T \eta_{pv} PF \quad (11)$$

where A_{PVcell} is the area of the PV cells of a collector.

The PV cell efficiency is estimated using Equation (12) below [12]:

$$\eta_{pv} = \eta_{nominal}\left[1 + Eff_T\left(T_{pv} - T_{ref}\right)\right]\left[1 + Eff_I\left(I_T - I_{ref}\right)\right] \quad (12)$$

where Eff_T and Eff_I are the dimensionless linear modifying factors; T_{ref} and I_{ref} are the reference temperature and irradiance level when the PV cells are at nominal efficiency ($\eta_{nominal}$).

The sky and cover exchange heat radiatively, and the radiative heat transfer coefficient is

$$h_{rs} = \sigma\,\epsilon_c\left(T_{c-kelvin} + T_{sky-kelvin}\right)\left(T^2_{c-kelvin} + T^2_{sky-kelvin}\right) \quad (13)$$

where $T_{c-kelvin}$ and $T_{sky-kelvin}$ are the cover and sky temperatures in K; σ is the Stefan–Boltzmann constant; ϵ_c is the emissivity of the glass cover.

The upper and lower surfaces of the air channel also exchange heat with each other, and the linearized coefficient is written as

$$h_{rad,\,u-l} = \frac{\sigma\left(T^2_{u-kelvin} + T^2_{l-kelvin}\right)\left(T_{u-kelvin} + T_{l-kelvin}\right)}{\frac{1}{\epsilon_u} + \frac{1}{\epsilon_l} - 1} \quad (14)$$

where $h_{rad,\,u-l}$ is the radiative heat transfer coefficient between the collector air channel's upper and lower surfaces; and $T_{u-kelvin}$ and $T_{l-kelvin}$ are the temperatures of lower and upper channels in K. σ is the Stefan–Boltzmann constant; ϵ_u and ϵ_1 are the emissivity of the internal channel's upper and lower surfaces.

The Reynolds number of the air channel is estimated as

$$Re = \frac{\frac{\dot{m}}{w\,d}D_h}{\mu} \quad (15)$$

where $\dot{m}$ is the air mass flowrate (kg/s), w is the width of the collector, d is the duct/channel height (m), and D_h is the hydraulic diameter of the BIPV/T-BISAH duct (m). In the case of a forced air laminar flow ($Re < 2300$), the Nusselt correlation is [18]

$$Nu = 4.9 + \frac{0.0606\,(Re\;Pr\;\;D_h/L)^{1.2}}{1 + 0.0909(Re\;Pr\;\;D_h/L)^{0.7}\;Pr^{0.17}} \quad (16)$$

For turbulent flow ($Re > 2300$),

$$Nu = 0.0158\ Re^{0.8} \tag{17}$$

Furthermore, for the first collector with turbulent flow, an additional term is included for abrupt contraction. For the first collector in a row where the air first enters the array, the Nusselt correlation is written as [12]

$$Nu = 0.0158\ Re^{0.8}\left[1 + \frac{C_x}{L/D_h}\right] \tag{18}$$

where C_x is the entrance effect factor, L is the collector length (m), and D_h is the hydraulic diameter of the duct. For the natural convection flowrate, the following relation was used [19]:

$$Nu = 1 + 1.44\left[1 - \frac{1708\left(sin(1.8\ slope)^{1.6}\right)}{Ra\ cos(slope)}\right]\cdot MAX\left[0,\ \left(1 - \frac{1708}{Ra\ cos(slope)}\right)\right] + MAX\left[0,\ \left(\frac{Ra\ cos(slope)^{\frac{1}{3}}}{5830}\right) - 1\right] \tag{19}$$

where

$$Ra = MAX\left[0,\ \left(\frac{g\ |\Delta T| d^3}{\left(\frac{T_u + T_l}{2}\right)\nu_{air}\alpha_{air}}\right)\right] \tag{20}$$

The slope is the tilt of the collector measured in radians from the horizontal, g is the acceleration constant, ΔT is the temperature difference between the upper and lower surfaces in the air channel, and ν_{air} and α_{air} are the kinematic (m^2/s) and dynamic ($kg/(m{\cdot}s)$) viscosity of the air, respectively.

For the heat transfer between the cover and the ambient air, the following correlation for the convective heat transfer correlation is used [20]:

$$h_c = 2.8 + 3V_W \tag{21}$$

The heat transfer coefficient, h_c, is in units of $W/(m^2{\cdot}K)$, and the wind velocity, V_W, is in units of m/s.

2.2. TBIPV/T Collector Energy Balance

Similarly to the OBIPV/T model, the energy balances of the TBIPV/T collector were established with the same assumptions and were in reference to Figure 1b.

About the cover, the energy balance is

$$\frac{T_{pv} - T_c}{R_g} = h_c(T_c - T_{amb}) + h_{rs}(T_c - T_{sky}) \tag{22}$$

The energy balance about the PV layer is

$$S_1 = \frac{T_{pv} - T_c}{R_g} + \frac{T_{pv} - T_u}{R_{pv-u}} \tag{23}$$

where S_1 is the net absorbed solar thermal flux at the PV layer for an TBIPV/T. Note R_{pv-u} is the R-value measured from the PV surface to the upper channel surface, just as it was in the OBIPV/T collector; however, for the TBIPV/T collector it consists of the PV cells and the glass backing.

The energy balance about the lower channel surface is

$$\frac{T_l - T_z}{R_{ins}} = h_a(T_a - T_l) + h_{rad,\ u-l}(T_u - T_l) + S_2 \tag{24}$$

where S_2 is the net solar thermal flux that passes through the pockets of glass between PV cells and is incident on the lower channel surface of the TBIPV/T collector.

The energy balance about the upper channel surface is

$$\frac{T_{pv} - T_u}{R_{pv-u}} = h_a(T_u - T_a) + h_{rad,\ u-l}(T_u - T_l) \tag{25}$$

The energy balance of the air flowing through the collector is

$$q = h_a(T_u - T_a) + h_a(T_l - T_a) \tag{26}$$

The net absorbed thermal radiation at the PV layer and at the lower surface of the air channel, as written by Kamel and Fung [21], are presented in Equations (27) and (28), followed by additional definitions of the terms and products in Equations (29)–(32).

$$S_1 = \tau_g\ \alpha_{pv}\ I_T\ (PF) - \eta_{pv}\ (PF)\tau_g\ I_T \tag{27}$$

$$S_2 = \alpha_l(1 - PF)\tau_g^2 I_T \tag{28}$$

In Equation (27), the τ_g and α_{pv} are the transmittance of the glass and absorptance of the PV cells, respectively; the product, $\tau_g\ \alpha_{pv}\ I_T\ (PF)$, is the solar irradiance absorbed by the PV layer. The second term, $\eta_{pv}\ (PF)\tau_g\ I_T$, is the electrical energy generated per panel area. In Equation (28), the solar irradiance travels through two glazing layers (hence, the $\tau_g^2 I_T$ term), and only through the pockets of glass $(1 - PF)$.

Lastly, τ_g is estimated using the following equations:

$$\tau_{\mathrm{g}} = \frac{\tau_{\mathrm{g,b}}\ I_B + \tau_{\mathrm{g,s}} I_S + \tau_{\mathrm{g,gr}} I_{GR}}{I_T} \tag{29}$$

$$\tau_{g,x} = \frac{\tau_{a,x}\ (1 - \rho_x)^2}{1 - (\rho_x\ \tau_{a,x})^2} \tag{30}$$

$$\tau_{a,x} = e^{-(Kl_g / cos\theta_{r,x})} \tag{31}$$

$$\rho_x = \frac{1}{2}\left(\frac{sin^2(\theta_{r,x} - \theta_x)}{sin^2(\theta_{r,x} + \theta_x)} + \frac{tan^2(\theta_{r,x} - \theta_x)}{tan^2(\theta_{r,x} + \theta_x)}\right) \tag{32}$$

where $\tau_{g,x}$ and ρ_x are the transmittance and reflectance for a particular solar radiation component (i.e., beam, sky diffuse, ground diffuse)

To fairly compare the performance of the TBIPV/T and the OBIPV/T collectors, the solar transmittance–absorptance model should be the same between the two models. Therefore, Equation (27) is rewritten as follows [17]:

$$S_1 = (\tau\alpha)_T\ I_T\ (PF) - (\tau\alpha)_T\ I_T\ (PF)\eta_{\mathrm{pv}} \tag{33}$$

where the $(\tau\alpha)_T\ I_T$ term is the same one found in Equation (8) of the OBIPV/T model. The modified TBIPV/T model with Equation (33) models the absorption of the solar irradiance at the PV layer in the same manner as the OBIPV/T. This same relationship can be applied to TBIPV/T even with its pockets of glass and PV cell area, because inherent to Equation (8) is the assumption that all radiation transmitted through the glass is absorbed at the PV layer (i.e., without further reflection). Because the transmittance–absorptance by the PV

layers is different from Kamel and Fung's model [21], the electrical power per panel area is modified as [17]

$$\frac{E_{pv}}{A_{panel}} = (\tau\alpha)_T \, I_T \, (PF)\eta_{\mathrm{pv}} \tag{34}$$

All convective and radiative coefficients of the TBIPV/T are estimated in the same manner as presented previously.

2.3. BISAH Energy Balance

Similarly to the OBIPV/T and TBIPV/T models, the energy balances of the BISAH were established with the same assumptions and references as in Figure 1c [17].

The energy balance about the top surface of the glass cover is

$$\frac{T_u - T_c}{R_g} = h_{rs}\left(T_c - T_{sky}\right) + h_c(T_c - T_{amb}) \tag{35}$$

The energy balance of the upper surface of the air channel is

$$h_{rad,\, u-l}(T_l - T_u) = \frac{T_u - T_c}{R_g} + h_a(T_u - T_a) \tag{36}$$

The energy balance of the control volume of air flowing through the collector is

$$q = h_a(T_u - T_a) + h_a(T_l - T_a) \tag{37}$$

The energy balance of the lower surface of the air channel is

$$\frac{T_z - T_l}{R_{ins}} + S_2 = h_a(T_l - T_a) + h_{rad,\, u-l}(T_l - T_u) \tag{38}$$

All parameters in Equations (35) and (38) have been explained earlier. All convective and radiative coefficients of the BISAH are estimated in the same manner as presented in the above sections.

2.4. Parametric Analysis of Collector System

A set of parametric analyses were conducted to determine the impact of the following parameters on the thermal-electric output of BIPV/T-BISAH systems:

- Internal channel surface emissivity (internal emissivity).
- Glass cover emissivity (cover emissivity).
- Collector arrangement in an array system.

These analyses were simulated using the modified version of EnergyPlus.

Different emissivity values were obtained using specific base material for the channel surface or by applying a surface coating. The emissivity parameters were analyzed in a single collector and series-row configuration to capture the full effect that a change in the parameters of a preceding collector may have on the following collector. This ensures that enhancements are identified for a system and not only a single collector.

Replacing a BIPV/T collector in a row with a BISAH yields lower electrical generation. But its addition may result in higher thermal performance [22], higher ASHP COP, and a net reduction in overall energy consumption. Similarly to the evaluation of the emissivity values, the impact that a BISAH has on the thermal–electric trade-off in a row of collectors is dependent on the conditions preceding it. The constant parameters of the OBIPV/T, TBIPV/T, and BISAH are listed in Table 1. Note that the cover emissivity (ϵ_c) values listed represent the fixed values when the internal emissivity (ϵ_u, and ϵ_l) are varied in the analysis; the reverse applies when the impact of cover emissivity is studied.

Table 1. OBIPV/T, TBIPV/T, and BISAH collector parameters.

Parameter	Value	Parameter	Value
K	4 m^{-1}	R_{ins}	1.9562 hr·m^2·K/kJ
l_g	0.0032 m	ϵ_c	0.6
n	1.526	ϵ_u	0.9
k_g	3.78 kJ/hr·m·K	ϵ_l	0.9
R_{pv-u} (OBIPV/T)	0.01 kJ/hr·m^2·K	PF	0.9
R_{pv-u} (TBIPV/T)	0.000847 kJ/hr·m^2·K	Collector (roof) tilt	35°
w	1.6 m	$\dot{m}$	0.1 kg/s
L	1 m	α_l	0.9
d	0.0635 m		

2.5. Modelling an Integrated BIPV/T-BISAH-ASHP System

A simple schematic of a BIPV/T system with an air source multispeed heat pump (MSHP) is shown in Figure 2. Hailu et al. [23] examined the integration of a constant-air flow BIPV/T system with an ASHP under Alaskan (U.S.A.) climate and suggested that lower flowrates could increase thermal performance for their system. Similarly, Delise and Kummert [24] simulated a BIPV/T coupled with an air-to-water heat pump by mixing a BIPV/T and outdoor air to ensure the combined flowrate was sufficient for the modelled heat pump. Tardif et al. [25] discovered that supplying 30% of the heat pump's required air flow from the BIPV/T reduced heating consumption savings. In these studies, modulating the total air flow through the BIPV/T based on environmental conditions could further enhance system performance. This would require an ASHP model that permits variable air flow on the source side.

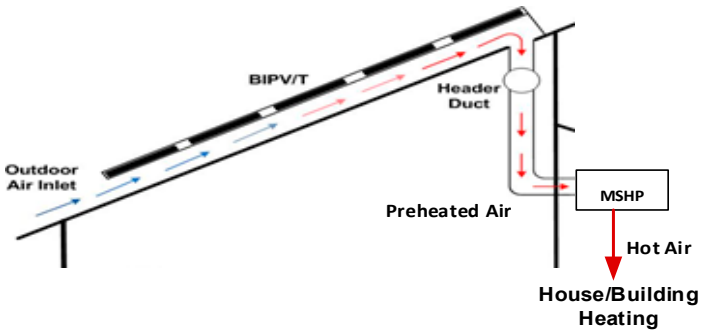

Figure 2. Schematic of working of BIPV/T with multispeed heat pump (MSHP).

EnergyPlus V8.0 is a robust open source program widely used by public and private organizations [26,27]. It provides a comprehensive list of residential equipment for modelling building designs. This makes it suitable for studying enhanced BIPV/T systems, as modifications and additional models can be implemented.

Models were written in FORTRAN to create a modified version of EnergyPlus V8.0. The modifications consisted of implementing quasi-steady state models of an OBIPV/T, TBIPV/T, and BISAH and modifications to the existing EnergyPlus Multispeed Heat Pump (MSHP) object (Coil:Heating:DX:Multispeed, a regression-based heat pump model [28]) to connect it to a BIPV/T-BISAH array.

A regression heat pump model requires performance data for a range of source flowrates and temperatures. However, manufacturers rarely provide these data because in normal operation, the source temperature does not fluctuate based on the outdoor unit's flowrate. Yet, in the integrated BIPV/T-BISAH-ASHP system, the flowrate determines the

exit temperature of the BIPV/T-BISAH array. In order to capture the impact of modulating the flowrate of the BIPV/T-BISAH array on the ASHP, the modified MSHP object assumes a mixture of BIPV/T array air and outdoor air to supply the manufacturer's total specified flowrate. Tardif et al. [25] applied the same approach using a constant 30% mixture. In the present study, the proportion was varied, and the additional fan power required was accounted, so that the integrated system could select a BIPV/T-BISAH flowrate to satisfy the heating load most efficiently.

The integrated system forms part of the building envelope, which in turns impact the heating load it attempts to satisfy. In the modified version of EnergyPlus, the envelope relies on a lagged temperature value of the interior surface of the zone ceiling (T_z). The simulation started by balancing the heat transfer of BIPV/T and BISAH surfaces. It then estimated the heating load for the house and simulated the performance of the multi-stage heat pump (MSHP). To avoid a computationally expensive iterative process between the envelope and HVAC simulation modules, a timestep sensitivity analysis was completed and found that a 20 min timestep offered a sufficiently steady T_z value, indicating that the use of the lagged value does not significantly impact the overall results.

3. Results and Discussions

3.1. TBIPV/T Collector Performance

Simulations of one row of six TBIPV/T collectors were conducted using the modified version of EnergyPlus for the heating season between 1 October and 21 May using weather data from Toronto, ON, Canada [29]. The collectors were arranged from the bottom of the roof to the ridge. The air flowed from the first collector upward to the ridge and exited the last collector. All the collector parameters are listed in Table 1.

3.1.1. Parametric Analysis: TBIPV/T—Internal Channel Surface Emissivity

For each simulation, a single emissivity value was applied to the upper and lower channel surfaces in every collector of the row (i.e., a single internal emissivity for all internal surfaces in the row). The annual thermal and electrical energy generation of the row of TBIPV/T collectors for a range of internal surface emissivity values are presented in Figure 3. The results show that the seasonal thermal generation increases from 1141 kWh to 1152 kWh, while electrical generation only increases by 1 kWh as the internal emissivity increases from 0.1 to 0.9. This suggests that a higher internal emissivity leads to better thermal–electrical performance of TBIPV/T collectors. Note that the magnitude of the changes is relatively small because of the low mass flowrate (0.1 kg/s) used in the analysis.

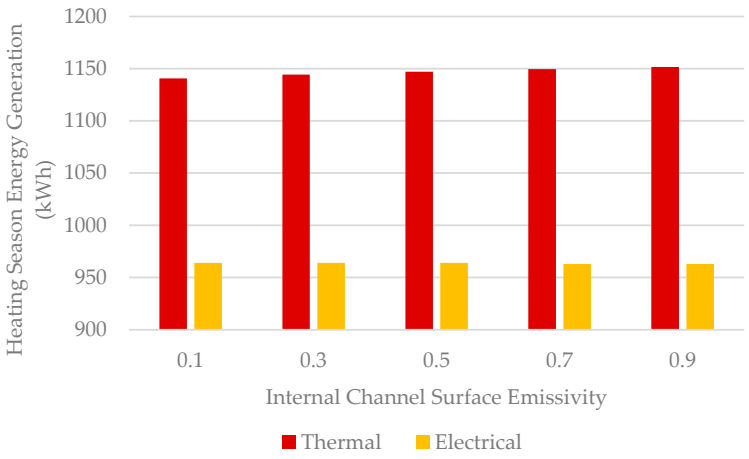

Figure 3. Heating season thermal and electrical generation of a row of TBIPV/T collectors with various internal channel emissivity values.

However, a review of the thermal energy generated on an individual collector basis suggests that the relationship is more intricate. The thermal generation of a row of six collectors with a high (0.9) and low (0.1) internal emissivity is shown in Figure 4. While the thermal generation of the first three high-internal-emissivity collectors (i.e., A1, A2, and A3) is greater than the corresponding low-emissivity collectors, the trend reverses for the final three collectors. The collectors (A4, A5, and A6) with a high internal emissivity generated less than the collectors with a low internal emissivity. This suggests that the impact of the internal emissivity of individual collectors depends on the position of the collector in the row. However, because the inlet temperatures of subsequent collectors after A1 in the high- and low-internal-emissivity rows are different, a comparison of the performance where the emissivity is the sole differentiator is needed.

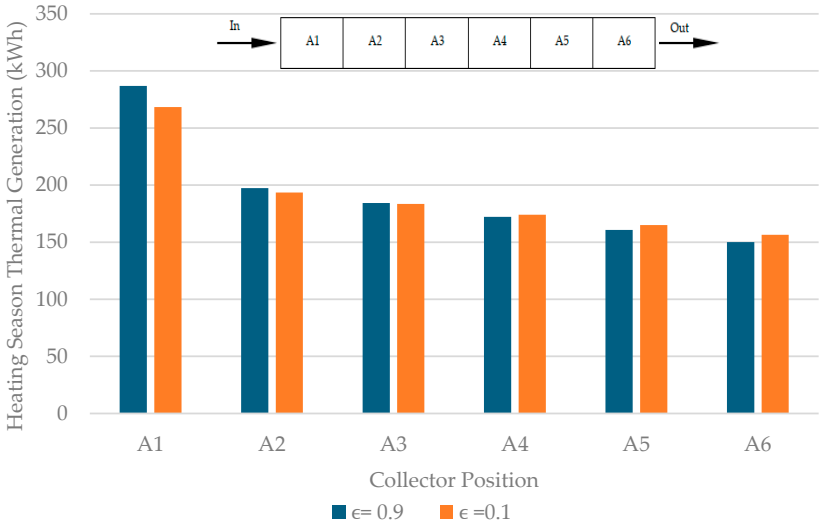

Figure 4. Heating season thermal generation of each TBIPV/T collector of a row with 0.9 and 0.1 internal emissivity values.

Figure 5 shows two sets of values for the hourly thermal generation of a single collector, one with an internal emissivity of 0.1 and the other with an emissivity of 0.9 from 9:00 to 17:00 (9 am to 5 pm) for a typical day (8 January). Overlayed is the temperature differential between the upper and lower air channel surfaces ($\Delta T = T_u - T_l$), where a positive value ($\Delta T > 0$) denotes the upper surface is warmer than the lower surface.

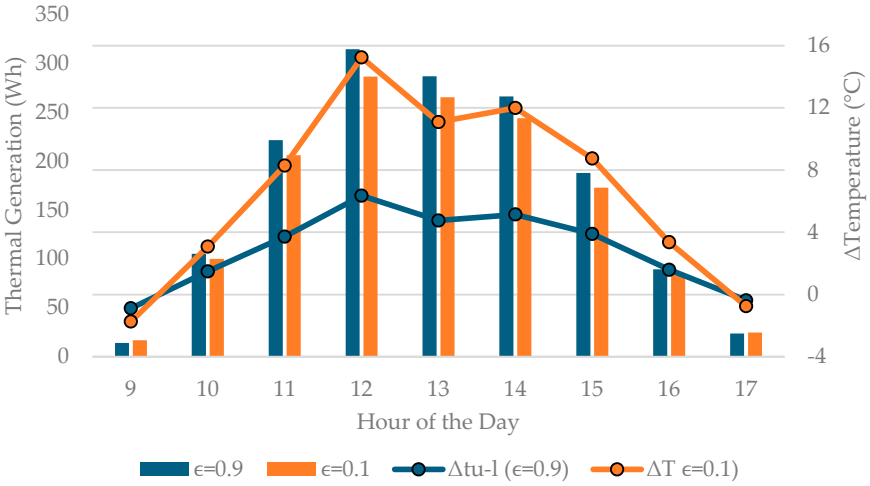

Figure 5. Hourly thermal generation and internal surface temperature differential of a TBIPV/T collector with 0.9 and 0.1 internal emissivity values.

The collector with an internal emissivity of 0.9 generated more thermal energy than the collector with an emissivity of 0.1 between 10:00 and 16:00 inclusive. This coincides when the upper channel surface is warmer than the lower channel surface ($\Delta T > 0$ or $T_u > T_l$). During these instances, a higher emissivity value improves internal longwave radiation between the two surfaces. As a result, more heat flows from the upper surface (warmer) to the lower surface (colder). The additional thermal energy received by the lower surface is mostly transferred to the air.

In contrast, when the upper surface is colder than the lower surface ($T_u < T_l$ or $\Delta T < 0$) at 9:00 and 17:00, the 0.1-internal emissivity collector generates more thermal energy. A lower internal emissivity reduces heat radiation from the lower to the upper surface, which allows the lower surface to retain more thermal energy.

As more thermal energy is retained in the lower surface, this causes the air stream to gain more thermal energy. Overall, a larger portion of the absorbed solar radiation by the collector is retained and less is lost through the glass cover to the surrounding environment. Concurrently, directing more thermal energy from the upper to the lower surface increases heat transfer from the PV layer, which decreases the PV temperature, resulting in increased electricity generation. The impact of the higher emissivity value is greater retention of the solar energy absorbed by the PV cell layer, and the collector generates greater thermal and electrical energy.

3.1.2. Internal Emissivity Design for TBIPV/T System

For the purpose of designing a TBIPV/T system, the decision to select a high or lower emissivity value depends on the frequency of the upper channel surface being warmer than the lower surface ($T_u > T_l$) and the magnitude of that differential (ΔT). For a TBIPV/T collector, that frequency and magnitude depend on its position along the row. Figure 4 shows that a high emissivity value (0.9) improves the performance of collectors A1–A3, but not all collectors benefited from a higher emissivity (as noted for A4–A6).

Therefore, an additional set of simulations were conducted to determine which collector configuration would benefit from high emissivity. Seven different row configurations were explored, with each row consisting of six collectors. All six collectors had an internal emissivity of 0.1 in the first-row configuration. In the second-row configuration, the first collector (A1) was equipped with an internal emissivity of 0.9, while collectors A2–A6 had an internal emissivity of 0.1. In the third row, A1 and A2 were equipped with an internal emissivity of 0.9, and A3–A6 remained unchanged with an internal emissivity of 0.1, and so on. In the final configuration, all six collectors had an internal emissivity of 0.9. Table 2 details the configurations and their corresponding heating season thermal generation. The heating season's electrical generation is excluded as the changes are insignificant.

Table 2. Heating season thermal generation of different row configurations of TBIPV/T collectors with internal emissivity values of 0.9 and 0.1.

$\epsilon_u = \epsilon_l = 0.9$	$\epsilon_u = \epsilon_l = 0.1$	Thermal Generation (kWh)
N/A	A1–A6	1141
A1	A2–A6	1155
A1–A2	A3–A6	1159
A1–A3	A4–A6	1161
A1–A4	A5 A6	1161
A1–A5	A6	1157
A1–A6	N/A	1152

Table 2 indicates that adjusting the internal emissivity values for the TBIPV/T systems based on the collector's position can lead to a single optimal configuration (maximum thermal and electrical generation). For the TBIPV/T system examined, the optimal configuration was to set the internal emissivity values of the first three collectors, which are closer to the inlet, to a high value, and the remaining three to low value.

3.1.3. Parametric Analysis: TBIPV/T—Cover Emissivity

The emissivity of the glass cover (Figure 1b) refers to its ability to emit thermal radiation when exposed to the sky. This study evaluated the performance of a single collector with three different cover emissivity values while maintaining the inlet temperature and other conditions constant. The results, in Figure 6, illustrates that as the cover emissivity increases, the total seasonal thermal energy generation decreases, while the total electrical energy generation slightly increases. Specifically, increasing the cover emissivity from 0.3 to 0.9 leads to a 23% decrease (47 kWh) in thermal energy generation and a 1.8% decrease (3 kWh) in electrical energy generation.

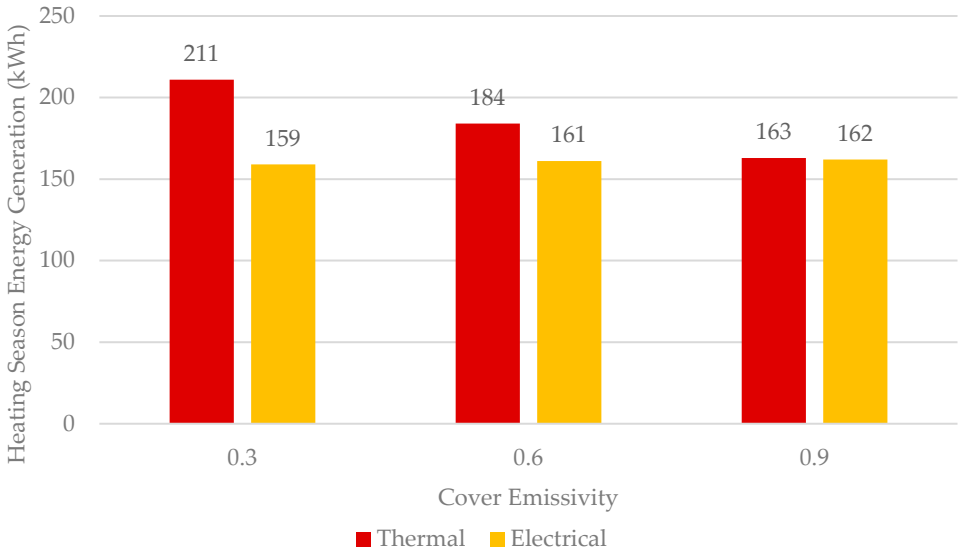

Figure 6. Heating season thermal and electrical generation of a single TBIPV/T collector with various cover emissivity values.

From a heat-loss perspective, as the cover emissivity is reduced, the longwave radiation between the sky and the cover diminishes. An analysis of a single collector (where all conditions were constant, including the inlet temperature except for the change in cover emissivity) shows that the reduced sky radiation results in lower radiative losses but higher convective losses; however, net losses to the environment decrease. Convective heat losses increase because reduced sky radiation leads to an increase in the cover temperature. Figure 7 shows this change for a collector with cover emissivity values of 0.6 and 0.3 on the chosen day (1 January) at 13:00. Although the total losses are similar, the collector with 0.3 cover emissivity does exhibit less heat loss.

Since the incident solar radiation for the two collectors at a chosen day/time is identical and the collector with a 0.3 cover emissivity loses less heat to the environment (Figure 7), it transfers more of the net absorbed radiation to the upper surface of the air channel. For the chosen day (1 January) at 13:00, the heat flux from the PV layer to the upper surface is shown in Figure 8, where the heat flux for the collector with 0.3 cover emissivity is greater than the collector with 0.6 cover emissivity.

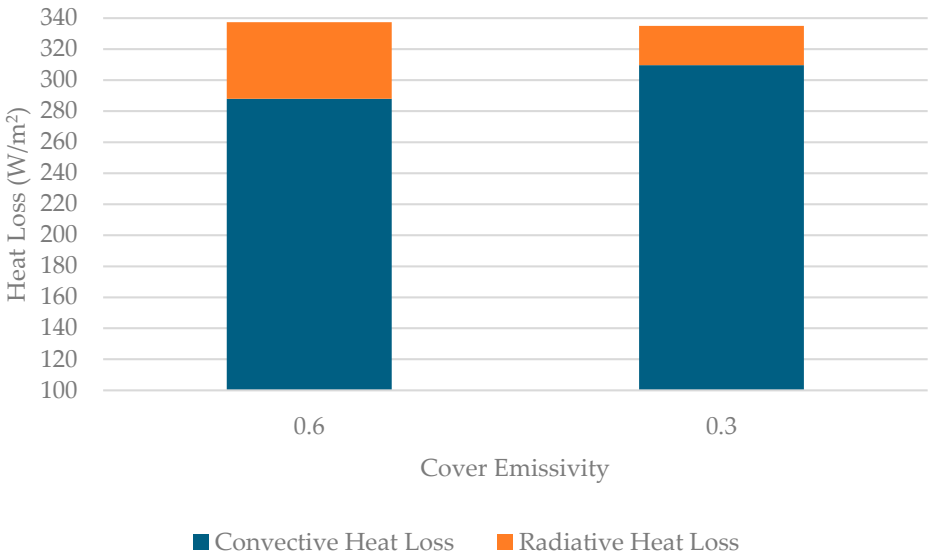

Figure 7. Total convective and radiative heat loss of a TBIPV/T collector with 0.6 and 0.3 cover emissivity values.

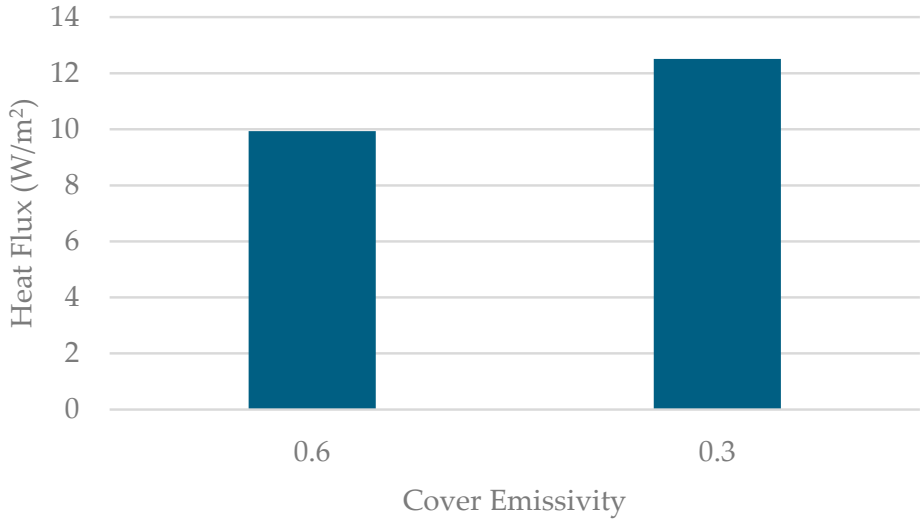

Figure 8. Heat flux from the PV layer to the upper surface of the air channel of a TBIPV/T collector with 0.6 and 0.3 cover emissivity values.

3.1.4. Cover Emissivity Design for TBIPV/T System

As the cover emissivity decreases, the net ambient heat loss (convective and radiative combined) decrease, the collector retains more of the absorbed solar energy, and its thermal generation increases. On the other hand, as more heat is retained at the PV layer, the PV cell temperature increases, and the electrical generation decreases. Although the exergy of electricity is higher, the analysis shows that lowering the cover emissivity from 0.9 to 0.1, over the heating season, increases the thermal energy by 367 kWh, while electrical generation decreases by 25 kWh, a ratio of approximately 14:1. Depending on the location of the system and its requirements, reducing cover emissivity may be a viable design option.

3.2. OBIPV/T Collector Performance

Simulations of one row of six OBIPV/T collectors were conducted using the modified version of EnergyPlus for the heating season between 1 October and 21 May using weather data from Toronto, ON, Canada [29]. The collectors were arranged from the bottom of the roof to the ridge. The air flowed from the first collector upward to the ridge and exited the last collector. All collector parameters are listed in Table 1.

3.2.1. Parametric Analysis: OBIPV/T—Internal Channel Surface Emissivity

The effect of increasing the internal emissivity of an OBIPV/T system is similar to its impact on TBIPV/T systems (see Section 3.1.1), where a high emissivity value leads to greater thermal and electrical generation. A similar analysis, completed using a single collector that illustrates this impact, is presented in Figure 9 (only the internal emissivity was varied). The improvement in performance is attributed to the same dynamics presented for TBIPV/T: high internal emissivity improves the inner longwave radiation heat transfer when the upper channel surface is warmer than the lower surface. This allows more thermal energy to be carried by the air stream, and less is lost to the environment. However, the electrical improvement is negligible.

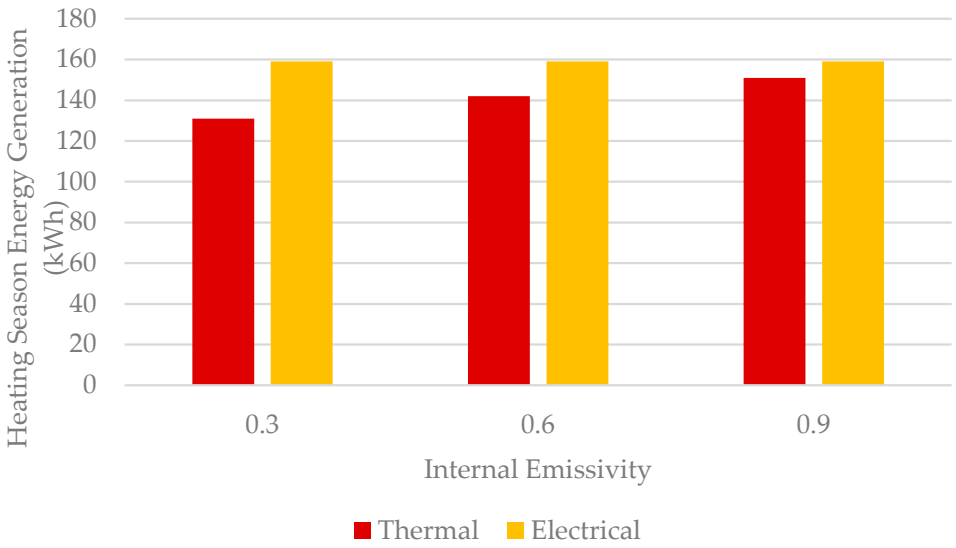

Figure 9. Heating season thermal and electrical generation of a single OBIPV/T collector with various internal emissivity values.

3.2.2. Internal Emissivity Design for OBIPV/T System

Unlike as shown in Section 3.1.2, where the optimal configuration of the TBIPV/T system identified is a combination of collectors with high and low internal emissivity values, the same analysis shows that the optimal OBIPV/T system configuration departs from this principle. The heating season results for seven different row configurations of six OBIPV/T collectors are summarized in Table 3; starting with a base configuration where all six OBIPV/T collectors have an internal emissivity of 0.1, each configuration was established by changing each subsequent collector's internal emissivity from 0.1 to 0.9 incrementally.

Table 3. Heating season thermal and electrical generation of different row configurations of OBIPV/T collectors with internal emissivity values of 0.9 and 0.1.

Collectors with $\epsilon_u = \epsilon_l = 0.9$	Collectors with $\epsilon_u = \epsilon_l = 0.1$	Thermal Generation (kWh)	Electrical Generation (kWh)
N/A	A1–A6	789	951
A1	A2–A6	813	952
A1–A2	A3–A6	839	953
A1–A3	A4–A6	864	953
A1–A4	A5–A6	889	954
A1–A5	A6	913	955
A1–A6	N/A	937	955

Table 3 illustrates that the best OBIPV/T configuration consists of identical collectors with a high internal emissivity, in contrast to the optimal TBIPV/T configuration that utilizes a combination of high- and low-internal-emissivity collectors. This difference is attributed to the "pockets of glass" between PV cells in TBIPV/T collectors, which OBIPV/T collectors lack.

In Section 3.1.2, it was shown that the use of a high or low internal emissivity for an individual collector was dependent on the frequency that the upper surface is warmer than the lower surface ($T_u > T_l$) and the magnitude of that differential (ΔT). In TBIPV/T collectors, the glass backing of the PV allows solar radiation to directly strike the lower channel surface, which increases its temperature. On the other hand, in an OBIPV/T collector, this radiation is absorbed by a tedlar layer, which increases the upper channel surface temperature and tends to leave the upper surface to be warmer than the lower surface ($T_u > T_l$). Following the greater tendencies of a warmer upper surface in OBIPV/T collectors, an optimal configuration is obtained using channel surfaces with a high emissivity.

3.2.3. Parametric Analysis: OBIPV/T—Cover Emissivity

Figure 10 displays the thermal and electrical energy produced by a single OBIPV/T collector during the heating season with different cover emissivity values. As the emissivity of the cover increases, the thermal generation decreases, while electrical generation increases. This trend is also observed in TBIPV/T collectors. Although net thermal generation decreases, a higher cover emissivity enables the collector to generate thermal energy for a longer duration over the day. For example, increasing the cover emissivity from 0.3 to 0.6 extends thermal energy generation by 208 h over the heating season, during early morning and late afternoon hours. The seasonal results indicate that the additional thermal generation at those hours are offset by the diminished thermal generation during higher solar hours.

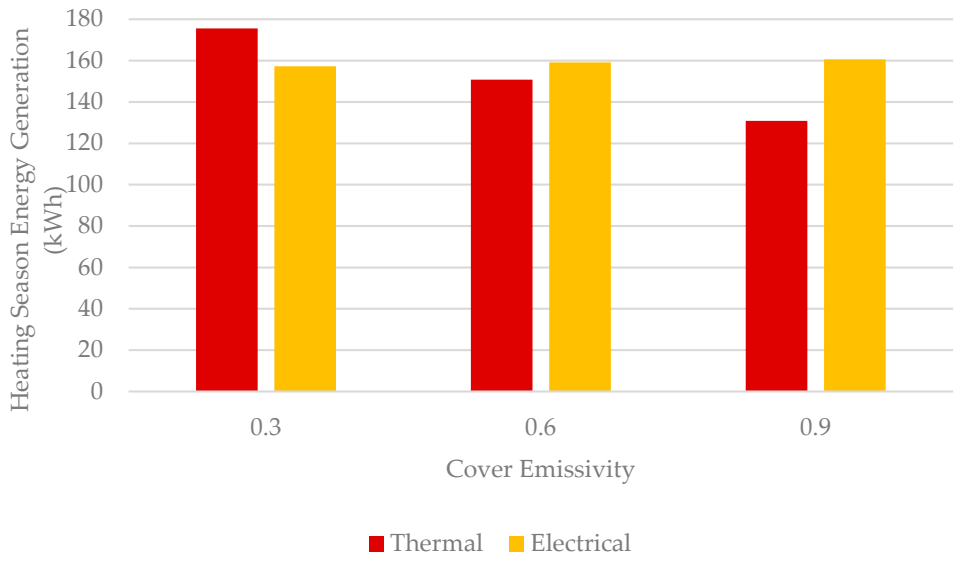

Figure 10. Heating season thermal and electrical generation of a single OBIPV/T collector with various cover emissivity values.

The impact of cover emissivity on the OBIPV/T system is similar to that on the TBIPV/T system (Figure 7). A low cover emissivity leads to a decrease in sky radiation loss and an increase in convective losses due to a higher cover temperature. But the net effect is a lower combined heat lost to the surroundings; this relationship is illustrated in Figure 11. As more of the absorbed solar radiation is retained within the collector, the temperature of the PV cells increases, leading to a reduction in electricity generation.

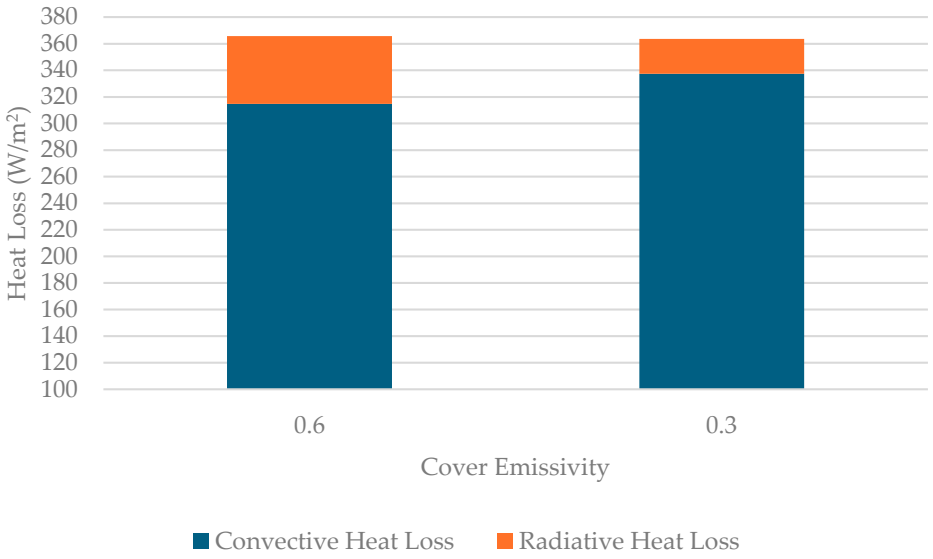

Figure 11. Total convective and radiative heat loss of an OBIPV/T collector with 0.6 and 0.3 cover emissivity values.

3.2.4. Cover Emissivity Design for OBIPV/T System

Different collectors with various cover emissivity values were combined to form seven configurations; these configurations are presented in Table 4. Starting with a base configuration where six OBIPV/T collectors have a cover emissivity of 0.9, each configuration was established by changing each subsequent collector's internal emissivity from 0.9 to 0.1. In the first configuration, all collectors had cover with an emissivity of 0.9. In the second configuration, the cover emissivity of A1 was changed to 0.1, while collectors A2 to A6 had a cover emissivity of 0.9. In the third configuration, the cover emissivity of A1 and A2 was 0.1, while A3 to A6 had a cover emissivity of 0.9, and so on. Table 4 also shows the findings from these configurations for the thermal and electrical energy produced during the heating season.

Table 4. Heating season thermal and electrical generation of different row configurations of OBIPV/T collectors with cover emissivity values of 0.9 and 0.1.

Collectors with ϵ_c = 0.1	Collectors with ϵ_c = 0.9	Thermal Generation (kWh)	Electrical Generation (kWh)
N/A	A1–A6	829	965
A1	A2–A6	887	960
A1–A2	A3–A6	938	955
A1–A3	A4–A6	993	950
A1–A4	A5–A6	1052	946
A1–A5	A6	1115	941
A1–A6	N/A	1182	936

The results of Table 4 do not reveal an optimal configuration, as determined in Table 2. Similar to the cover emissivity design for a TBIPV/T system in Section 3.1.4, a single optimal design where both thermal and electrical generation are maximized based on cover emissivity does not exist; since the cover emissivity has a direct correlation with the thermal generation and an inverse relationship with the electrical generation, respectively. However, these results provide alternative options, including the trade-off between increasing thermal generation at the expense of reducing electricity generation. The results show that when

the cover emissivity is decreased from 0.9 to 0.1, the thermal energy generation increases by 352 kWh, while the electrical energy generated decreases by 29 kWh. This is approximately 12:1, in contrast to the 14:1 ratio that the TBIPV/T exhibited.

3.3. BISAH Collector Performance

This section examined the impact of internal channel emissivity and cover emissivity parameters on a BISAH system (see Figure 1c). The parameters of the BISAH collector used for the analysis are detailed in Table 1. The results highlight the impact of the internal and cover emissivity on BISAHs. The heat transfers are more prominently observed in the BISAH compared to the BIPV/T system, for the same flowrate; therefore, the analysis presented also serves to highlight the trends seen in the transparent and opaque BIPV/T collectors.

3.3.1. Internal Channel Surface Emissivity Impact on BISAH

Figure 12 presents the thermal energy a single collector generates over the heating season.

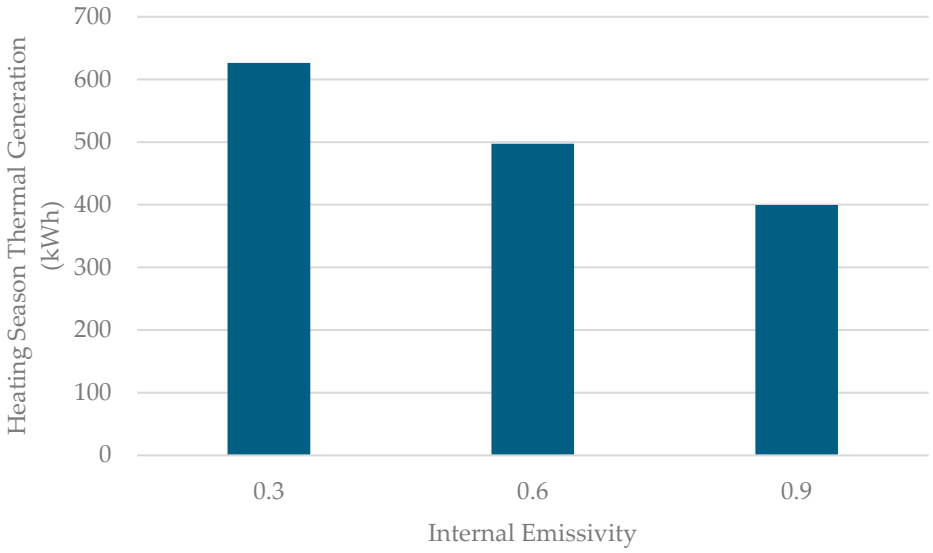

Figure 12. Heating season thermal generation of a single BISAH with various internal emissivity values.

The trend of higher thermal generation by a single BISAH for low values of internal emissivity is similar to the relationship exhibited in TBIPV/T collectors. Based on the earlier explanation, when the lower surface is warmer than the upper surface, a low internal emissivity reduces the internal longwave radiation heat transfer from the lower surface to the upper surface. As shown in Figure 13, the heat flux is reduced by approximately 50% as the internal emissivity of a BISAH is reduced from 0.9 to 0.3. As a result, less thermal energy is lost through the cover, a higher portion of the solar energy collected is retained at the lower surface, and more thermal energy is transferred to the air stream.

Furthermore, as the lower surface is warmer than the upper surface for most sunlight hours, this eliminates the need to analyze rows that contain collectors with a different internal emissivity. A simulation of two rows of a BISAH, one with a high internal emissivity and the other equipped with a low emissivity, was conducted. The results are presented in Figure 14 and show that optimal thermal generation is achieved utilizing a low internal emissivity value and not by combining a BISAH with different internal emissivity values.

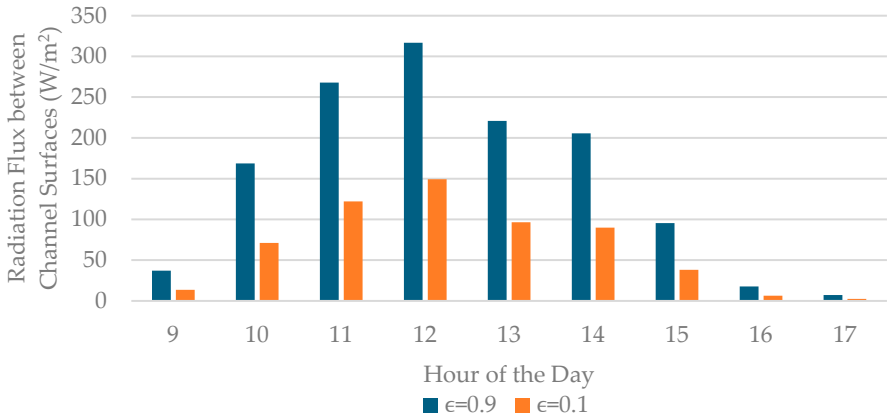

Figure 13. Hourly internal longwave radiation heat transfer from the lower surface to the upper surface in a BISAH with 0.9 and 0.1 internal emissivity values.

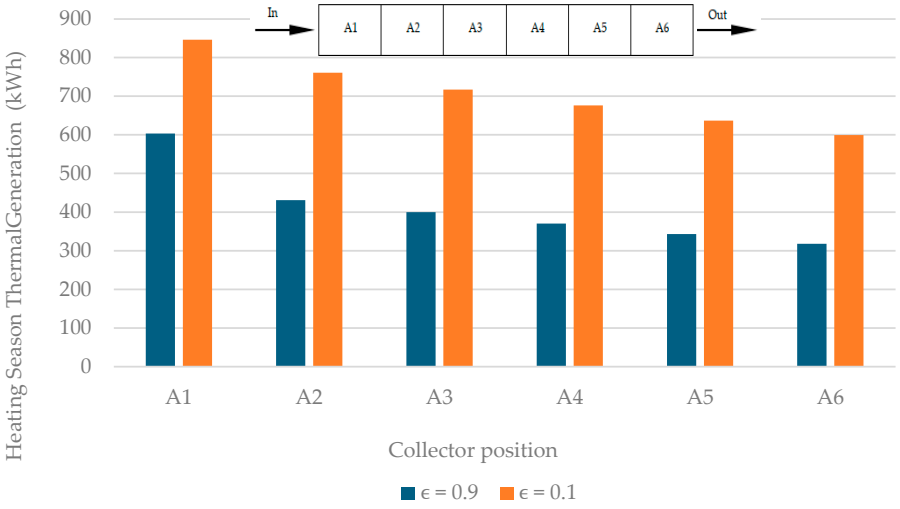

Figure 14. Heating season thermal generation of each BISAH of a row with 0.9 and 0.1 internal emissivity values.

Figure 15 shows the thermal energy generated during the heating season by a single row of BISAH collectors for different emissivity values. The results indicate that reducing the internal emissivity from 0.9 to 0.1 increases the thermal energy gained by 1771 kWh, resulting in a 72% performance increase.

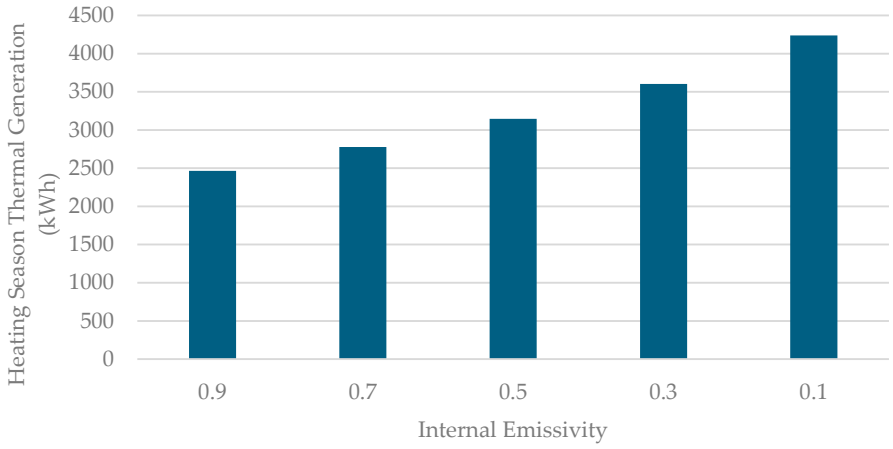

Figure 15. Heating season thermal generation of a row of BISAH with various internal emissivity values.

3.3.2. Glass Cover Emissivity Impact on BISAH

The impact of the cover emissivity on the thermal generation of BISAHs is similar to the impact identified for transparent and opaque BIPV/T collectors. As shown in Figure 16, an increase in cover emissivity reduces the thermal energy generated by a single BISAH, whereas a low emissivity value allows the collector to generate more heat during the day and in the early and late afternoon hours.

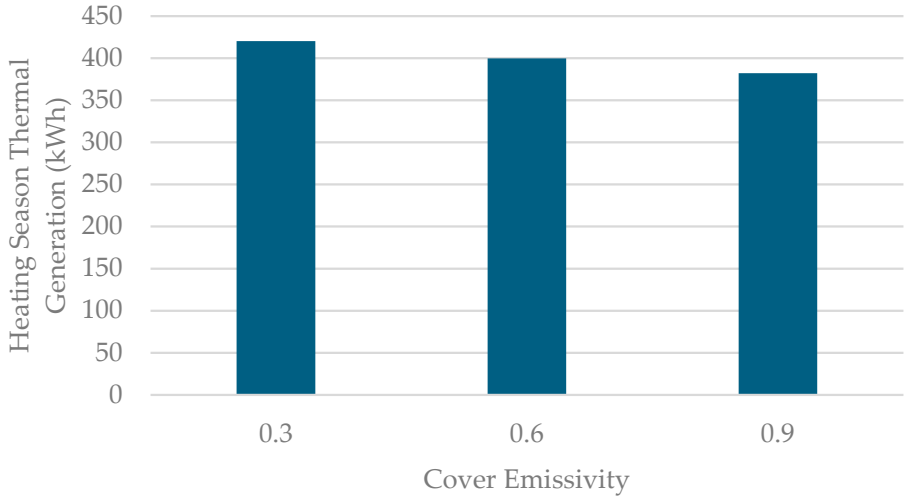

Figure 16. Heating season thermal generation of a single BISAH with various cover emissivity values.

A reduction in the cover emissivity of the BISAH collector decreases overall losses to the environment, as depicted in Figure 17. However, not all energy savings are transferred to the air stream. Summing the savings over the day reveals that reducing the cover emissivity reduces heat loss by 69 kWh. The air stream only gains 68 kWh, and the zone gains an additional 1 kWh.

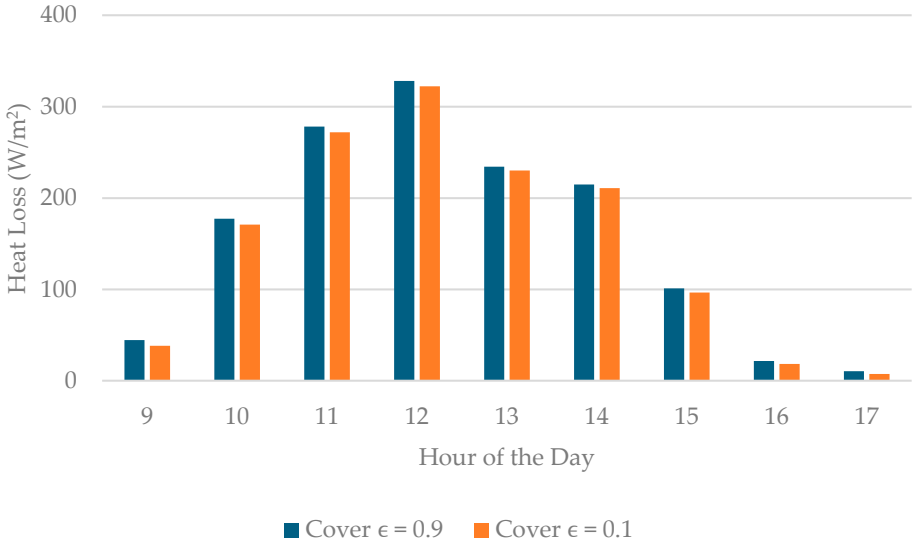

Figure 17. Hourly total convective and radiative heat loss of a BISAH with 0.9 and 0.1 cover emissivity values.

Following the principle explained in Sections 3.1.4 and 3.2.4, combining collectors with different cover emissivity values does not yield a higher performing configuration than applying a single low or high emissivity value, as supported in Figure 18 and as

illustrated in Figure 19, as reducing the emissivity from 0.9 to 0.1 for all collectors in a row simultaneously increases the thermal generation by 12%, from 2375 kWh to 2662 kWh.

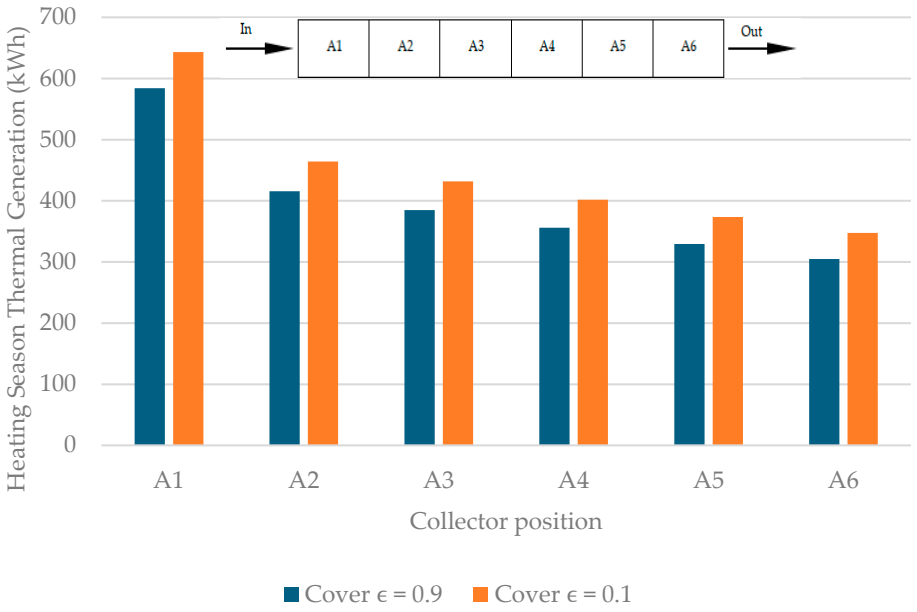

Figure 18. Heating season thermal generation of each BISAH of a row with 0.9 and 0.1 cover emissivity values.

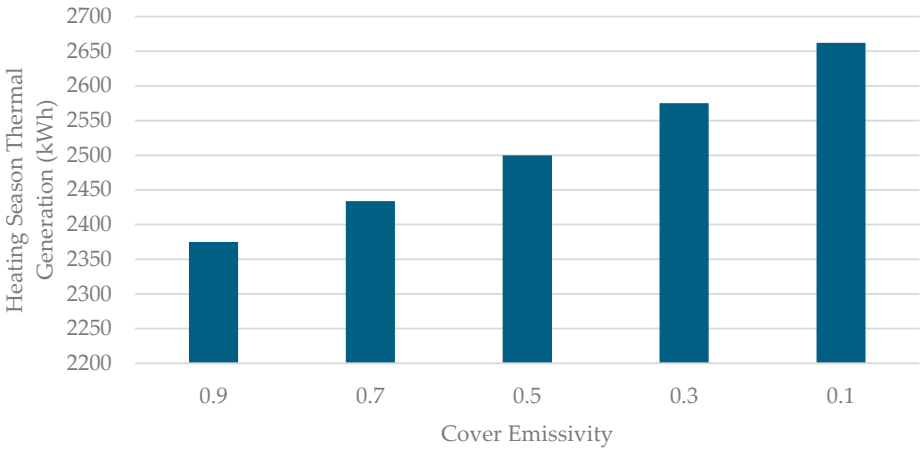

Figure 19. Heating season thermal generation of a row of BISAH with various cover emissivity values.

3.4. OBIPV/T and TBIPV/T Integration with BISAH

In an effort to improve the efficiency of BIPV/T—ASHP systems, parametric analyses on collector arrangements were conducted. The objective was to identify additional enhancements that would increase performance with a limited increase in fan power, as researchers found that adding vertical collectors at the end of a BIPV/T system is challenging when the air flow is directed upward along a building facade, as it requires increased fan power due to the change in air flow angle [11,30,31].

An OBIPV/T array system can be improved by including a BISAH at the end of each row to boost the air temperature before it exits the system. The analysis focused on an individual 5-OBIPV/T collector row, as presented in Figure 20a, followed by the same row enhanced with one and two BISAH, as shown in Figure 20b,c, respectively. Array-level results were obtained by applying a multiple to the results presented for each row. These three arrangements were simulated in Toronto, ON, Canada, each with a common collector

tilt of 35°, *PF* of 0.85, and constant flowrate of 0.2 kg/s for each row (all other parameters are presented in Table 1). The energy generation is presented in Table 5 on a per-row basis.

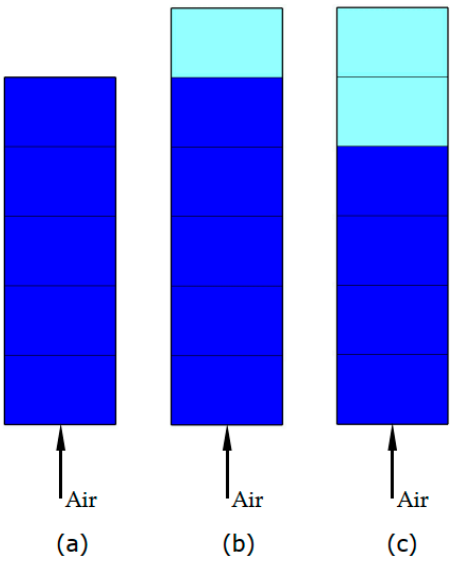

Figure 20. One row of (**a**) 5 OBIPV/T collectors (dark blue), (**b**) 5 OBIPV/T collectors (dark blue) with 1 BISAH (light blue), (**c**) 4 OBIPV/T collectors (dark blue) with 2 BISAH (light blue).

Table 5. Summary of the thermal and electrical energy generated by the 5 OBIPV/T, 5 OBIPV/T + 1 BISAH, and 4 OBIPV/T + 2 BISAH rows during the heating season.

Row Configuration	Thermal Generation (kWh)	Electrical Generation (kWh)
5 OBIPV/T	1118	758
5 OBIPV/T + 1 BISAH	1965	758
4 OBIPV/T + 2 BISAH	2597	607

Through a heating season simulation (Table 5), it was observed that a single row of five OBIPV/T collectors produced 1118 kWh of thermal energy and 758 kWh of electricity. The addition of a single BISAH increased thermal generation by 846 kWh, which represents a 76% boost in thermal generation, while electrical generation remained unchanged. On the other hand, further modification of this configuration, as shown in Figure 20c, resulted in 2597 kWh of thermal energy and 607 kWh of electrical energy. The ratio of additional thermal generation to the reduction in electrical generation for this combination is approximately 4:1, illustrating diminishing marginal returns on thermal generation for a reduction in electrical generation.

Buildings with limited roof area that are unable to accommodate an additional BISAH may consider the application of a TBIPV/T system. An analysis to determine the comparable TBIPV/T for a given OBIPV/T + BISAH system was conducted. The configurations evaluated are presented in Figure 21. A basic five OBIPV/T collector (1.6 m × 1 m) row was established, and differently sized BISAHs were included as an enhancement to form Row OB-1 to OB-3. Row T-1 to T-2 correspond to TBIPV/T rows, where the PF was set to allow the same net glazing area (sum of all pockets of glass) as the total BISAH area in Row OB-1 to OB-3. To fairly compare the electrical generation, the same PFs were also applied to the OBIPV/T + BISAH rows. All other parameters are presented in Table 1.

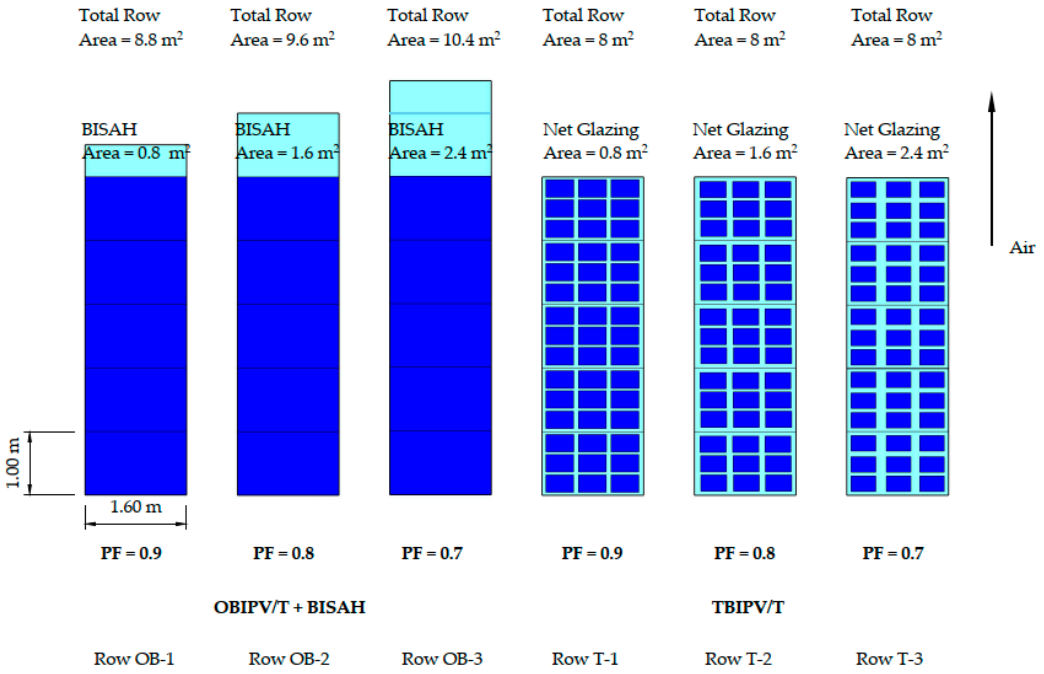

Figure 21. Schematic of OBIPV/T + BISAH rows and the corresponding TBIPV/T rows (equivalent net glazing area). Solid dark blue denotes OBIPV/T collectors, light blue signifies BISAH, and dark blue grid-pattern represents TBIPV/T collectors.

The results of these six configurations are presented in Table 6. A comparison of the opaque and transparent rows shows that the TBIPV/T rows generated 8% to 31% less thermal energy and 1% to 3% more electricity than the OBIPV/T + BISAH rows with the corresponding *PF* (0.9 to 0.7). Individually, TBIPV/T collectors are more efficient on a per-area basis compared to the OBIPV/T because they allow solar radiation to strike the air channel directly, which allows the collector to retain more absorbed solar energy. For a *PF* of 0.8 and 0.7, the TBIPV/T row's marginal thermal gain is less than the thermal generation attributed to the BISAH, as shown through a comparison of thermal energy generated per total row area. Although Row T-1 generates more thermal energy on a row area basis, overall, Row OB-1 generates more energy, as a result of a larger total area.

Table 6. Heating season thermal and electrical generation of Rows OB-1 to OB-3 and Rows T-1 to T-3.

Row ID	PF	Thermal Generation (kWh)	Thermal Generation Per Row Area (kWh/m^2)	Electrical Generation (kWh)
OB-1	0.9	1535	174	804
OB-2	0.8	1975	206	713
OB-3	0.7	2407	231	623
T-1	0.9	1407	176	814
T-2	0.8	1535	192	727
T-3	0.7	1662	208	639

Note that the cover emissivity of the TBIPV/T in Figure 21 was not optimized; the results from Section 3.1.4 suggest that a lower emissivity could improve the thermal generation with limited degradation in electrical performance. Rows T-1 to T-3 were modified into T-4 to T-6, with $\epsilon_c = 0.1$. The results of these enhanced TBIPV/T rows are presented in Table 7.

Table 7. Heating seasons thermal and electrical generation of Rows T-4, T-5, and T-6.

Row ID	PF	Thermal Generation (kWh)	Thermal Generation Per Total Row Area (kWh/m^2)	Electrical Generation (kWh)
TB-4	0.9	1679	210	803
TB-5	0.8	1797	225	718
TB-6	0.7	1913	239	631

The results show that the TBIPV/T rows are now more efficient (per row area) than the original OBIPV/T + BISAH rows, whereas Row T-1 generated 8% less thermal energy than OB-1, the enhanced Row T-4 (with the same PF = 0.9) generated 9% additional thermal energy over the heating season instead, and electrical generation only decreased by less than 0.5%. On the other hand, TB-5's and TB-6's total generation remained less than that of OB-2 and OB-3, respectively, even though the enhanced TBIPV/T rows were more efficient on a per area. This is attributed to the simply larger overall area of OB-2 (9.6 m^2) and OB-3 (10.4 m^2) compared to that of the TBIPV/T rows (8 m^2).

The analysis conducted highlights the enhancement of OBIPV/T with BISAHs to attain improved performance and the potential for optimized TBIPV/T collectors to deliver comparable performance while requiring less roof area, which results in lower fan power requirements.

3.5. Net-Zero Energy (NZE) House Equipped with an Integrated BIPV/T-MSHP System

A system of six rows of BIPV/T-BISAH coupled with an MSHP was implemented in a NZE house and simulated in Toronto, ON, Canada, for the heating season using the modified version of EnergyPlus. The integrated system is shown schematically in Figure 22. Each row contained five TBIPV/T collectors and a single BISAH at the end, resulting in a 36-collector system. The BIVP/T—BISAH system preheats outdoor air through six air channels and delivers it to the outdoor unit of the MSHP. The air flow controller adjusts the proportion of BIPV/T heated air and unheated outdoor air by selecting a BIPV/T air flowrate from a discrete set of pre-defined flowrates, with the objective to meet the heating demand placed on the MSHP with the lowest combined HP and fan power consumption.

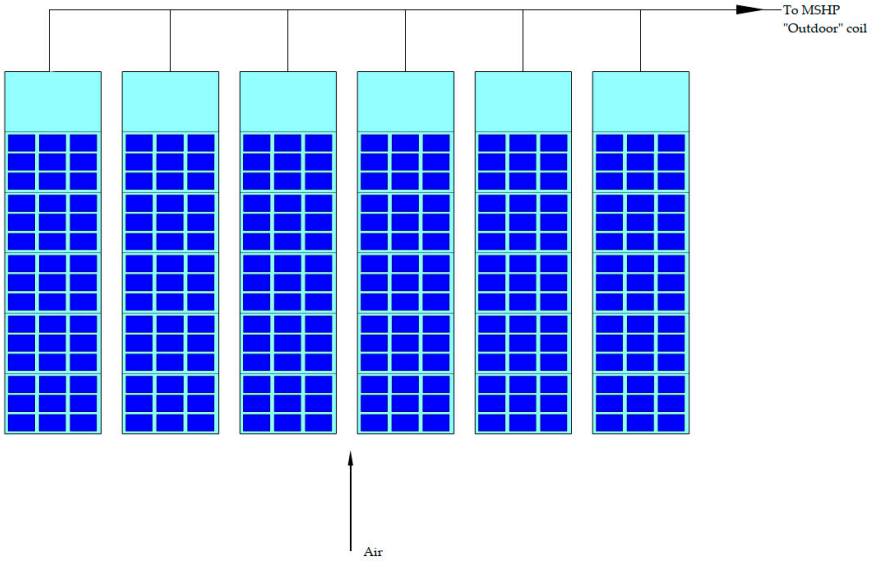

Figure 22. Array of 36 BIPV/T-BISAH collectors coupled with an MSHP. Dark blue grid-pattern denotes TBIPV/T collectors, while solid light blue signifies BISAH.

3.5.1. NZE Construction and BIPV/T + BISAH System

The parameters for the TBIPV/T and BISAH collectors are given in Table 8. A description of the construction details of the proposed NZE house is presented in Table 9, and a Sketchup model of the house is shown in Figure 23.

Table 8. TBIPV/T collector and BISAH parameters coupled with the MSHP.

TBIPV/T Collector		BISAH Collector	
K	4 m^{-1}	K	4 m^{-1}
l_g	0.0032 m	l_g	0.0032 m
n	1.526	n	1.526
k_g	3.78 kJ/hr·m·K	k_g	3.78 kJ/hr·m·K
R_{pv-u}	0.000847 kJ/hr·m^2·K	w	1.6 m
w	1.6 m	L	1 m
L	1 m	d	0.0635 m
d	0.0635 m	R_{ins}	1.9562 hr·m^2·K/kJ
R_{ins}	1.9562 hr·m^2·K/kJ	ϵ_c	0.6
ϵ_c	0.6	ϵ_u	0.1
ϵ_u	0.9	ϵ_l	0.1
ϵ_l	0.9	α_l	0.9
PF	0.9		
α_l	0.9		

Table 9. NZE house construction detail.

Parameter	Parameter Value
Wall U-value	0.135
Roof U-value	0.113
Floor U-value	0.222
Window U-value	2.61
BIPV/T roof tilt	35°
BIPV/T roof direction	South
Building volume	460 m^3
Gross floor area	182 m^2

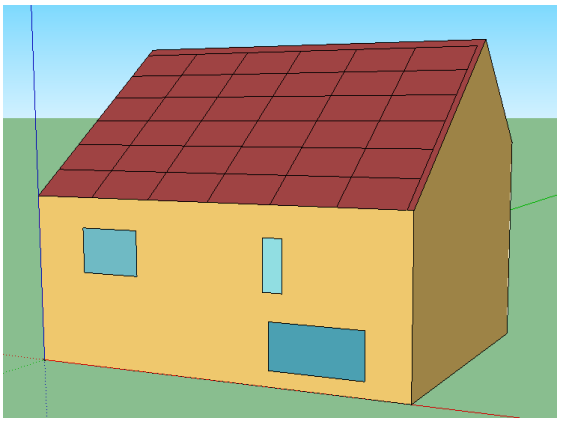

Figure 23. Sketchup model of the NZE house.

3.5.2. NZE HVAC System

The HVAC system consisted of a constant air volume (CAV) system, an energy recovery ventilator (ERV), and a variable-capacity multi-stage heat pump (MSHP). The system operates an on-and-off fan–compressor system, where the fan and compressor cycle in unison to respond to the heating load. The rated capacity and flowrate (indoor and outdoor) and the parameters of the MSHP used in the simulation are summarized in Table 10.

Table 10. MSHP simulation parameters for the NZE house.

Maximum Speed Parameters	Value	Minimum Speed Parameters	Value
Rated capacity [1]	3460 W	Rated capacity [1]	2126
Rated COP [1]	4.7	Rated COP [1]	5
Rated indoor air flowrate	0.213 m^3/s	Rated indoor air flowrate	0.118 m^3/s
Constant outdoor air flowrate	0.637 m^3/s	Constant outdoor air flowrate	0.637 m^3/s

[1] Rating conditions: 8.3 °C outdoors, 21 °C indoors. In order to combine the two air streams, as described in Section 2.5, the simulation used one fan to draw air through the BIPV/T-BISAH array and another for direct outdoor air. The two air streams are mixed and then fed to the MSHP. The purpose is to ensure that the source-side flowrate of the MSHP matches the specifications that the performance regression was developed under; other studies have applied the same method as well [24,25]. The parameters for the BIPV/T-BISAH fan and the outdoor air fan are outlined in Table 11. Performance coefficients were sourced from EnergyPlus V8.0's dataset.

Table 11. BIPV/T-BISAH and outdoor air supply variable speed fan parameters.

BIPV/T-BISAH Fan		Outdoor Air Supply Fan	
Fan Parameter	**Value**	**Fan Parameter**	**Value**
$\Delta P_{design,\ PVT}$	42 Pa	$\Delta P_{design,\ Outdoor\ Air}$	2 Pa
$\dot{m}_{design}\left(\dot{m}_{HP}\right)$	0.75 kg/s	$\dot{m}_{design}\left(\dot{m}_{HP}\right)$	0.75 kg/s
η_{fan}	0.9	η_{fan}	0.9
c_1	0.35071223	c_1	0.35071223
c_2	0.30850535	c_2	0.30850535
c_3	−0.54137364	c_3	−0.54137364
c_4	0.8718823	c_4	0.8718823
c_5	0	c_5	0

3.5.3. NZE House: Modelling Results

This section presents a comparison of the performance of the NZE house with the MSHP and with and without a BIPV/T-BISAH system. In the base case, the MSHP produced 4300 kWh of thermal energy to meet the heating demand over the heating season in Toronto, ON, Canada, and consumed 1258 kWh of electricity, resulting in a seasonal COP of 3.41. When the house was equipped with the BIPV/T-BISAH-MSHP system, the MSHP produced 4067 kWh of thermal energy and consumed 1169 kWh of electricity, while the additional BIPV/T fan consumed 7 kWh of electricity. This resulted in a seasonal COP of 3.46. Overall, the BIPV/T-BISAH-MSHP system reduced space heating electricity consumption by 6.5% over the heating season.

For 29 December, the BIPV/T-BISAH operated continuously from 10:00 to 16:00. Figure 24 shows the modulated BIPV/T-BISAH system air flowrate and the outdoor air flowrate. It is evident that most of the flowrate is delivered by the BIPV/T-BISAH system. On average, the BIPV/T-BISAH supplied 71% of the required air flowrate of the MSHP. On this day, this proportion yielded the lowest total energy consumption.

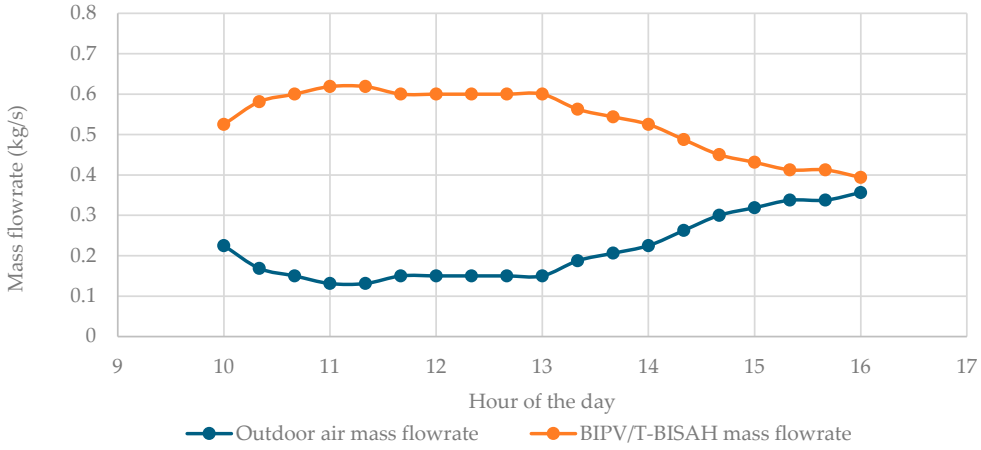

Figure 24. Hourly BIPV/T-BISAH array and outdoor air flowrate for 29 December.

The BIPV/T-BISAH system preheats the air and mixes it with outdoor air to form mixed air. This is then diverted to the MSHP. The effective MSHP source temperature (mixed temperature) is shown in Figure 25.

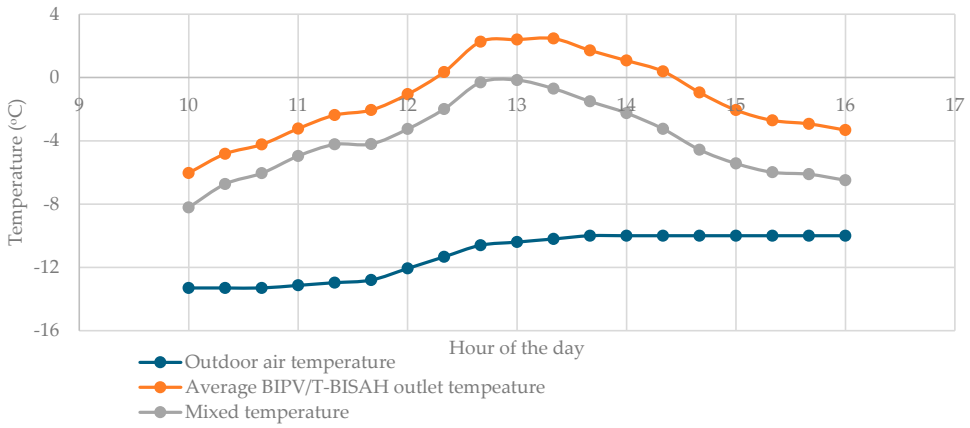

Figure 25. Hourly outdoor air temperature and the BIPV/T-BISAH array's average outlet and mixed air temperatures for 29 December.

The corresponding electricity consumption of the BIPV/T-BISAH coupled MSHP system and the MSHP in the base case for this day are shown in Figure 26.

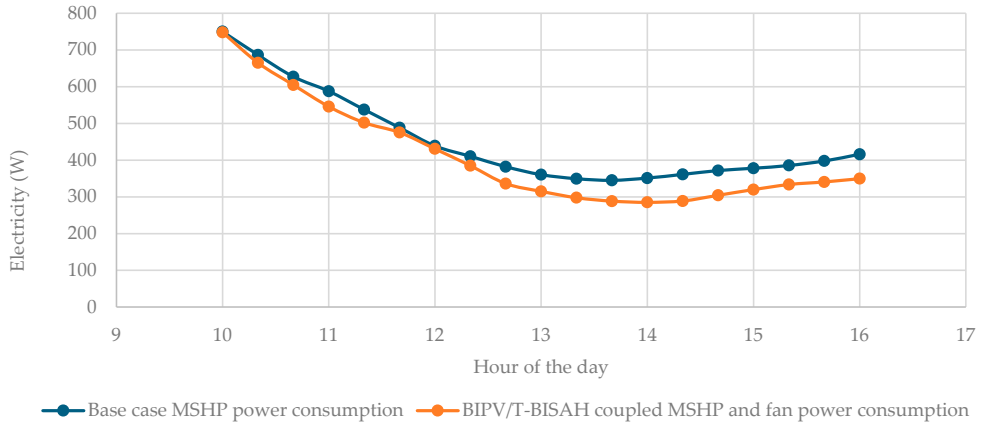

Figure 26. Hourly BIPV/T-BISAH coupled MSHP and base case MSHP electricity consumption for 29 December.

3.5.4. Limitations of Energy Savings

The BIPVT/-BISAH system was utilized for approximately 431 h throughout the 2524 h of sunlight (i.e., solar irradiance greater than 0 W/m^2) or 17%. From the literature, other researchers have only simulated the operation of flow-modulated BIPV/T systems when solar irradiance was greater than 50 W/m^2 [25], this was likely the minimum level required to overcome the thermal inertia of the system. After normalizing based on the hours when irradiance was greater than 50 W/m^2, the BIPV/T-BISAH system operated for 23% of the time.

The limited energy savings is attributed to the low utilization rate of the BIPV/T-BISAH system by the controller. First, due to the energy-efficient nature of the house, the seasonal heating demand is low, which limits the hours when the system can operate. Heating is often required during early morning and late afternoon/evening hours, where solar radiation is limited and the BIPV/T-BISAH system is only able to generate a limited amount of energy. Second, due to the limitation of available heat pump performance data relating the outdoor/source flowrate to the heating capacity, this study did not consider the performance of the heat pump with excess source flowrate. Improving the heat pump's source side heat transfer could potentially reduce the compressor power consumption and yield higher net energy savings.

4. Conclusions

This study simulated OBIPV/T, TBIPV/T, BISAHs, and their integration with a flow-modulated MSHP using a modified version of EnergyPlus. Analyses were conducted to assess the impact of an individual collector's air channel surface and glass cover emissivity value on the collector's thermal–electrical performance. An investigation was completed, evaluating the impact of the arrangement of OBIPV/T, TBIPV/T, and BISAH collectors in a single row. These culminated in a heating season simulation of an integrated BIPV/T-BISAH-MSHP system.

This study found that the performance of different types of solar collectors can be improved using specific internal and cover emissivity values. High internal emissivity values benefit OBIPV/T collectors, while a row of TBIPV/T collectors benefit from a combination of high and low values. For both types of collectors, the optimal internal emissivity value enhances heat transfer from the PV layer and upper air channel surface to the lower channel surface, which allow the collectors to retain more solar energy. On the other hand, lowering the cover emissivity increases thermal generation and decreases electricity generation, for both BIPV/T collector types. This is attributed to reduced longwave radiation between the collector's cover and the environment, which also results in increased thermal energy retention by the collector. This simultaneously also increases PV temperature, which reduces electrical generation.

The analysis of collector arrangements for OBIPV/T, TBIPV/T, and BISAHs showed that the placement of the collectors significantly affects overall performance. Adding a BISAH at the end of a row of OBIPV/T collectors improved performance, but in some cases, enhanced TBIPV/T collectors performed just as well while requiring less area and fewer collectors.

During a heating season simulation, the BISAH-BISAH-MSHP system reduced electricity consumption by 6.5% (82 kWh) for an NZE house in Toronto. This reduction was due to passive house features limiting heating demand during the day when the BIPV/T-BISAH is most efficient, reducing the overall utilization rate of the BIPV/T-BISAH system.

Extension of This Study

It is essential to explore the integration of building-integrated photovoltaic/thermal (BIPV/T) systems with a BIPV/T-coupled air source heat pump (ASHP) and thermal storage systems for future energy-efficient homes. This integration addresses the discrepancy between the availability of solar energy and the demand for space heating. By coupling the BIPV/T-ASHP system with thermal storage, the design can increase the system's overall utilization and create additional energy saving opportunities and integration with other systems. Future studies should consider developing a connection between the BIPV/T-BISAH system and a domestic hot-water heat pump to improve overall energy efficiency when space heating is not required in energy-efficient homes. Finally, establishing a control strategy that integrates the BIPV/T-BISAH array system with the ASHP, thermal storage, and hot-water heat pump will be crucial for optimizing energy in these systems.

Author Contributions: A.S.F.: responsible for conceptualizing research ideas, supervising the research project, providing research resources (including funding), and approving the final content draft of the paper; E.V.: responsible for conducting the literature survey, developing the methodology, modelling on EnergyPlus, analyzing data, drawing conclusions, and preparing the preliminary draft of the paper; R.K.: responsible for analyzing data and the final writing, reviewing, editing, and submission of the paper. All authors have read and agreed to the published version of the manuscript.

Funding: One of the authors (Edward Vuong) thanks the Ontario Graduate Scholarship, MITACS, Ryerson International, Yeates School of Graduate Studies, CUPE, and Ryerson Student Union for their financial support. Funding from the Natural Sciences and Engineering Research Council (NSERC) of Canada Discovery Grant is gratefully acknowledged.

Data Availability Statement: Data are confidential and will be made available upon request.

Acknowledgments: One of the authors (Edward Vuong) thanks the Ontario Graduate Scholarship, MITACS, Ryerson International, Yeates School of Graduate Studies, CUPE, and Ryerson Student Union for their financial support. The authors also thank the Toronto and Region Conservation Authority (TRCA) and its staff for their help in this research. Funding from the Natural Sciences and Engineering Research Council (NSERC) of Canada Discovery Grant is gratefully acknowledged.

Conflicts of Interest: The authors declare that they have no known competing financial interests or personal relationships that could have appeared to influence the work reported in this paper.

Abbreviations

BIPV/T	building-integrated photovoltaic–thermal
TBIVT/T	transparent building-integrated photovoltaic–thermal
OBIPV/T	opaque building-integrated photovoltaic–thermal
BISAH	building-integrated solar air heater
MSHP	multi-stage heat pump
ASHP	air source heat pump
COP	Coefficient of Performance
PV	photovoltaic
PF	packing factor
ERV	energy recovery system
NZE	net zero-energy
GHG	greenhouse gas
Nomenclature	
A_{panel}	Collector area (m^2)
$A_{PV\ cell}$	Total area of the PV cells for one PV panel (m^2)
c_1, c_2, ... c_5	Fan power coefficient
C_x	Entrance effect factor

D	Duct height (m)
D_h	Hydraulic diameter of BIPV/T-BISAH duct (m)
E_{pv}	Electricity generation power (W)
Eff_I	PV linear modifying factor—irradiance
Eff_T	PV linear modifying factor—temperature
g	Acceleration constant (9.81 m/s^2)
h_a	Convective heat transfer coefficient of air within the BIPV/T-BISAH channel (W/m^2·K)
h_c	Convective heat transfer coefficient for the wind and cover (W/m^2·K)
$h_{rad,\ u-l}$	Radiative heat transfer coefficient between the collector air channel's upper and lower surface (W/m^2·K)
h_{rs}	Radiative heat transfer coefficient the cover and the sky (W/m^2·K)
I	Solar irradiance on a surface (W/m^2)
K	Glazing extinction coefficient (m^{-1})
l_g	Glazing thickness (m)
L	Collector length (parallel to the direction of flow) (m)
$\dot{m}$	Air mass flowrate (kg/s)
Nu	Nusselt number
PF	PV cell packing factor
Pr	Prandtl number
q	Heat flux to air stream in collector (W/m^2)
Ra	Rayleigh number
Re	Reynolds number
R_g	R-value of glazing (m^2·K/W)
R_{pv-u}	R-value measured from PV layer to the upper surface of the air channel of a collector (m^2·K/W)
R_{ins}	R-value of roof insulation (m^2·K/W)
S	Net absorbed solar thermal flux at the PV layer for an OBIPV/T collector (W/m^2)
S_1	Net absorbed solar thermal flux at the PV layer for a TBIPV/T collector (W/m^2)
S_2	Net absorbed solar thermal flux at the lower surface for a TBIPV/T collector (W/m^2)
T_a	Average air temperature through the collector (°C)
T_{amb}	Temperature of ambient/outdoor air (°C)
T_c	Temperature of the cover (°C)
$T_{c-kelvin}$	Temperature of the cover in Kelvin (K)
T_l	Temperature of the lower channel surface (°C)
$T_{l-kelvin}$	Temperature of the lower channel surface (K)
T_{pv}	Temperature of the PV layer (°C)
$T_{pvt,i}$	Average BIPV/T-BISAH array outlet temperature for a particular timestep (°C)
T_{ref}	Reference temperature for PV model (25 °C)
T_{sky}	Sky temperature (°C)
$T_{sky-kelvin}$	Sky temperature (K)
T_u	Temperature of the upper air channel surface (°C)
T_z	Interior zone surface temperature (°C)
V_W	Wind speed (m/s)
w	Width of collector (dimension perpendicular to air flow) (m)
Greek Symbols	
α_{air}	Thermal diffusivity of air (m^2/s)
α	Solar absorptance
ΔP	Fan pressure rise (Pa)
ΔT	Temperature difference between the channel's upper and lower surfaces ($T_u - T_l$) (°C)

ϵ_c	Emissivity of the glass cover
ϵ_l	Emissivity of the internal channel's lower surface
ϵ_u	Emissivity of the internal channel's upper surface
η_{fan}	Nominal fan power efficiency
$\eta_{nominal}$	Nominal PV cell efficiency
η_{pv}	PV cell efficiency
$\theta_{r,x}$	Refractive radiation angle for a solar component x
θ_x	Radiation angle for a solar component x
ρ_x	Reflectance for a particular radiation component x
σ	Stefan–Boltzmann constant
τ	Transmittance through the glass
$\tau\alpha$	Transmittance–absorptance product
μ	Dynamic viscosity (kg/m·s)
ν	Kinematic viscosity (kg/m·s)

References

1. NRCan. *Energy Efficiency Trends in Canada*; NRCan: Ottawa, ON, Canada, 2016.
2. Environment and Climate Change Canada. *Greenhouse Gas Sources and Sinks in Canada. National Inventory Report 1990–2016*; Environment and Climate Change Canada: Ottawa, ON, Canada, 2023. Available online: https://www.canada.ca/en/environment-climate-change/services/climate-change/greenhouse-gas-emissions/sources-sinks-executive-summary-2023.html (accessed on 29 April 2024).
3. O. Reg. 350/06: Building Code. Available online: https://www.ontario.ca/laws/regulation/060350 (accessed on 3 February 2017).
4. Canada's National Energy Code. Available online: https://natural-resources.canada.ca/energy-efficiency/buildings/new-buildings/canadas-national-energy-code/20675 (accessed on 13 December 2024).
5. Abbasi, M.H.; Abdullah, B.; Ahmad, M.W.; Rostami, A.; Cullen, J. Heat transition in the European building sector: Overview of the heat decarbonisation practices through heat pump technology. *Sustain. Energy Tech. Assmt.* **2021**, *48*, 101630. [CrossRef]
6. Abdelrazik, A.S.; Shboul, B.; Elwardany, M.; Zohny, R.N.; Osama, A. The recent advancements in the building integrated photovoltaic/thermal (BIPV/T) systems: An updated review. *Renew. Sustain. Energy Rev.* **2022**, *170*, 112988. [CrossRef]
7. Kumar, R.; Rosen, M. A critical review of photovoltaic–thermal solar collectors for air heating. *Appl. Energy* **2011**, *88*, 3603–3614. [CrossRef]
8. Yang, H.; Liu, X.; Wang, C.; Shen, C.; Han, R.; Kalogirou, S.A.; Wang, J. Investigation on the heating performance of a BIPV/T façade coupled with direct-expansion heat pump system in severe cold region. *Renew. Energy* **2024**, *232*, 121065. [CrossRef]
9. Kamel, R.; Fung, A.S.; Dash, P.R.H. Solar systems and their integration with heat pumps: A review. *Energy Build.* **2015**, *87*, 395–412. [CrossRef]
10. Wang, X.; Xia, L.; Bales, C.; Zhang, X.; Copertaro, B.; Pan, S.; Wu, J. A systematic review of recent air source heat pump (ASHP) systems assisted by solar thermal, photovoltaic and photovoltaic/thermal sources. *Renew. Energy* **2020**, *146*, 2472–2487. [CrossRef]
11. Bae, S.; Chae, H.; Nam, Y. Experimental analysis of an integrated system using photovoltaic–thermal and air source heat pump for real applications. *Renew. Energy* **2023**, *217*, 119128. [CrossRef]
12. Kamel, R.S.; Fung, A.S. Modeling, simulation and feasibility analysis of residential BIPV/T + ASHP system in cold climate-Canada. *Energy Build.* **2014**, *82*, 758–770. [CrossRef]
13. Zhao, Y.; Li, W.; Zhang, G.; Li, Y.; Ge, M.; Wang, S. Experimental performance of air-type BIPVT systems under different climate conditions. *Sustain. Energy Technol. Assess.* **2023**, *60*, 103458. [CrossRef]
14. Payne, W.V.; Yoon, S.H.; Domanski, P.A. *Heating Mode Performance Measurements for a Residential Heat Pump with Single Faults Imposed*; NIST: Gaithersburg, MA, USA, 2009.
15. Bergene, T.; Lovvik, O.M. Model calculations on a flat-plate solar heat collector with integrated solar cells. *Sol. Energy* **1995**, *55*, 453–462. [CrossRef]
16. U.S. Department of Energy (DOE). *EnergyPlus*; V8.0; Software; Ernest Orlando Lawrence Berkeley National Laboratory: Berkeley, CA, USA, 2013. Available online: https://github.com/NREL/EnergyPlusRelease/releases/tag/8.0.0.008 (accessed on 8 September 2024).
17. Vuong, E. Thermal Enhancement of a Building Integrated Photovoltaic/Thermal System Coupled with an Air Source Heat Pump. Master's Thesis, Ryerson University, Toronto, ON, Canada, 2017. [CrossRef]
18. Mercer, W.E.; Pearce, W.M.; Hitchcock, J.E. Laminar Forced Convection in the Entrance Region between Parallel Flat Plates. *ASME J. Heat Transf.* **1967**, *89*, 251–256. [CrossRef]

19. TRNSYS17. *TESSLibs 17 Component Libraries for the TRNSYS Simulation Environment Volume 03: Electrical Library Mathematical Reference*; Thermal Energy System Specialist: Madison, WI, USA, 2013; p. 82.
20. Watmuff, J.H.; Charters, W.S.; Proctor, D. Solar and Wind Induced External Coefficients for Solar Collectors. *COMPLES* **1977**, *2*, 56.
21. Kamel, R.S.; Fung, A.S. Modelling and characterization of transparent building integrated PV/T collector. *Energy Procedia* **2015**, *78*, 1871–1876. [CrossRef]
22. Cartmell, B.; Shankland, N.; Fiala, D.; Hanby, V. A multi-operational ventilated photovoltaic and solar air collector: Application, simulation and initial monitoring feedback. *Sol. Energy* **2004**, *76*, 45–53. [CrossRef]
23. Hailu, G.; Dash, P.; Fung, A.S. Performance evaluation of an air source heat pump coupled with a building-integrated photovoltaic/thermal (BIPV/T) system under cold climatic conditions. *Energy Procedia* **2015**, *78*, 1913–1918. [CrossRef]
24. Delisle, V.; Kummert, M. Cost-benefit analysis of integrating BIPV-T air systems into energy-efficient homes. *Sol. Energy* **2016**, *136*, 385–400. [CrossRef]
25. Tardif, J.M.; Tamasauskas, J.; Delisle, V.; Kegel, M. Performance of air based BIPV/T heat management strategies in a Canadian home. *Proc. Environ. Sci.* **2017**, *38*, 140–147. [CrossRef]
26. Excell, L.E.; Nutkiewicz, A.; Jain, R.K. Multi-scale retrofit pathways for improving building performance and energy equity across cities: A UBEM framework. *Energy Build.* **2024**, *324*, 114931. [CrossRef]
27. Ejenakevwe, K.A.; Song, L. Investigation of smart thermostat fault detection and diagnosis potential for air-conditioning systems using a Modelica/EnergyPlus co-simulation approach. *Energy Build.* **2024**, *309*, 114053. [CrossRef]
28. Group—Heating and Cooling Coils: Input Output Reference—EnergyPlus 8.0. Available online: https://bigladdersoftware.com/epx/docs/8-0/input-output-reference/page-042.html#coilheatingdxmultispeed (accessed on 13 December 2024).
29. Climate. One Building. Available online: https://climate.onebuilding.org/WMO_Region_4_North_and_Central_America/CAN_Canada/ON_Ontario/CAN_ON_Toronto.Pearson.Intl.AP.716240_CWEC.zip (accessed on 13 December 2024).
30. Pantic, S.; Candanedo, L.; Athienitis, A.K. Modeling of energy performance of a house with three configurations of building-integrated photovoltaic/thermal systems. *Energy Build.* **2010**, *42*, 1779–1789. [CrossRef]
31. Maghrabie, H.M.; Elsaid, K.; Sayed, E.T.; Abdelkareem, M.A.; Wilberforce, T.; Olabi, A.G. Building-integrated photovoltaic/thermal (BIPVT) systems: Applications and challenges. *Sustain. Energy Technol. Assess.* **2021**, *45*, 101151. [CrossRef]